Full Length Article

A fully coupled multidomain and multiphysics model for evaluation of shale gas extraction

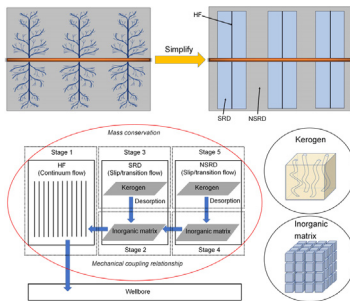Wai Li[a], Jishan Liu[a,*], Jie Zeng[a], Yee-Kwong Leong[a], Derek Elsworth[b], Jianwei Tian[a], Lin Li[a]

[a] School of Engineering, The University of Western Australia, Perth, WA 6009, Australia
[b] Department of Energy and Mineral Engineering, G3 Centre and Energy Institute, The Pennsylvania State University, University Park, PA 16802, USA

GRAPHICAL ABSTRACT

ARTICLE INFO

ABSTRACT

Creating a stimulated reservoir domain (SRD) is a necessity to effectively extract natural gas from shale reservoirs. After hydraulic fracturing, a shale reservoir has three distinct domains: SRD, non-stimulated reservoir domain (NSRD) and hydraulic fractures (HFs). In previous studies, the property contrasts and interactions between different domains are often not fully considered. In this study, a fully coupled multi-domain and multi-physics model is developed to incorporate these complexities. The shale reservoir is characterized as an assembly of three distinct components: organic kerogen, inorganic matrix and HF. Furthermore, the kerogen and inorganic matrix are defined as dual-porosity-dual-permeability media, while the HF is simplified as a 1-D cracked medium. Particularly, the inorganic matrix has different properties in each of the SRD and NSRD to reflect the stimulation effect of hydraulic fracturing on the near-HF matrix. Under this framework, a series of partial differential equations (PDEs) fully coupled by mass transfer and mechanical deformation relations were derived to define various processes in the shale reservoir. These PDEs were numerically solved by the finite element method. The proposed model is validated against analytical solutions and verified against gas production data from the field. Sensitivity analyses reveal: (1) that both size and internal structure of the SRD significantly affect gas extraction by improving SRD properties and in creating low-pressure zones around the NSRD; (2) that the NSRD determines the sustainability of gas production; and (3) that the change of mechanical properties in one domain affects the evolution of transport properties in the entire reservoir.

* Corresponding author.
  E-mail address: Jishan.liu@uwa.edu.au (J. Liu).

1. Introduction

Extracting natural gas from organic-rich shale formations is becoming an important issue in the oil and gas industry due to its enormous success in North America over the last two decades [1,2]. The current boom in shale gas exploitation is substantially attributed to the progress in horizontal well drilling and massive hydraulic fracturing (fracking) technologies [3]. The former accesses a large reservoir volume, while the latter creates numerous fractures and cracks as gas flow channels [4,5]. These treatments for shale reservoirs allow gas to be released from ultra-tight shale [6]. Despite a few successful exploitation cases, uncertainty about how much gas can be recovered from shale reservoirs is still an issue [2]. This uncertainty originates from the complexities of shale gas production and our inability to fully understand the effects of heterogeneous, multi-domain, and multi-physics characteristics of shale reservoirs [7]. Although there are some existing simulators for shale gas extraction [8,9,10,11,12], how to incorporate various mechanisms and interactions in shale reservoirs remains a significant challenge [13].

One of the complexities of shale reservoirs is heterogeneity. Differing from conventional sandstone reservoirs (mainly containing inorganic minerals), gas shale matrix is composed of kerogen pockets (organic matter) within inorganic matrix (referred to as IM, the combination of clay and detrital minerals) [14,15]. Although both kerogen and IM have extremely low permeability, there are significant differences between them: (1) Kerogen has a relatively higher porosity (often > 5%, up to 50%) than that of IM (normally in the range $2\% - 8\%$) [16,17]; (2) A large amount of gas is adsorbed on the kerogen surface while adsorption in the inorganic matrix is negligible [18]; (3) Most of the pores in the kerogen can be approximately deemed as tortuous capillaries while slot-shape fractures are widely distributed in the IM [19], which implies that the compressibilities of these two components are very different [20]. In order to accurately describe the heterogeneity of shale, dual-porosity (considering kerogen and IM containing natural fractures as two interacting pressure systems) or triple-porosity models (considering kerogen, IM and natural fractures as three interacting pressure systems) have been established based on the continuum assumption, and have been successfully used in modelling [13,21].

Multi-domain characteristic is another essential complexity of shale reservoirs. Hydraulic fracturing not only creates a set of primary hydro-fractures (HFs) with millimetre-scale apertures, but also enhances the permeability of the shale matrix near HFs by initiating numerous secondary hydro-fractures and activating the original natural fractures. An illustration of a hydraulically fractured shale formation with HFs and secondary hydro-fractures is shown in Fig. 1(a). The shale matrix with enhanced permeability caused by these secondary hydro-fractures, is referred to as a "stimulated reservoir domain" (SRD) in this study. The fractures in the SRD typically have apertures ranging from nanometre-level to submillimetre-level [22]. In contrast, the non-stimulated reservoir domain (NSRD) is not modified by fracking, and retains all the original properties of the shale reservoir [23]. Therefore, a producing shale gas reservoir consists of three distinct domains: (1) HF; (2) SRD and (3) NSRD. It is clear that describing this multi-domain characteristic is important for modelling shale gas production since the property contrasts between these domains will lead to differences in production performance. Unfortunately, most previous studies ignore the existence of an SRD, or impractically simplify this domain. For instance, the SRD and HF have been abstracted [24] into a set of 1-D fractures, and the remainder of the reservoir is considered as uniform [Fig. 1(b)]. This method may cause some problems because the equivalent properties of these abstracted (virtual) fractures are not easy to define, and neglecting the difference between the near-HF matrix and the far-from-HF matrix will lead to deviation of the simulation results from the actual situation. Another example is that of considering the SRD as a continuous domain [23] occupying the entire space between HFs

[Fig. 1(c)]. However, the actual SRD is sometimes not so well-connected due to the limitation of hydraulic fracturing efficiency and cost, which cannot be reflected by the model. To overcome this drawback, analytical models have been proposed [25] in which the SRD is composed of a series separated sub-SRDs partly occupying the space between HFs. Each sub-SRD encloses an HF [Fig. 1(d)]. This model [25] successfully describes s discontinuous SRD, and includes the situation in Fig. 1(c) because the SRD becomes a continuous domain when the width of the sub-SRD is equal to the HF spacing. Despite the advantage in geometry, their model only incorporated the difference between SRD and NSRD in permeability, while the contrasts of other pore properties (e.g., porosity) and mechanical properties (e.g., rock compressibility) were not considered. Their model also neglected some other important mechanisms and effects, such as rock deformation, desorption and the flow regime. Therefore, the existing descriptions of multi-domain characteristics of shale reservoirs should be improved to achieve more accurate modelling and simulation.

The third complexity within a producing shale gas reservoir is that multiple physical processes with feedbacks occur within this system. First, the mechanical deformation of shale is a significant influencing factor in stress-sensitive shale gas plays [26,27,28]. The evolution of effective porosity and apparent permeability are related to the stress dependence of the reservoir. In the second place, gas desorption in kerogen supplies gas flow and induces sorptive strain [7,29]. Desorption also influences the effective porosity of the kerogen for gas flow by changing the thickness of adsorbed gas layer, which is referred to as a "volumetric effect" [30,31]. In addition, the gas flow regime in shale may vary from continuum flow to slip flow and transition flow due to the extremely small pores/cracks in the shale matrix, which influences the apparent permeability of the matrix [32,33]. These mechanisms should be considered to accurately describe the gas production process in shale reservoirs.

In this study, a series of fully coupled partial differential equations (PDEs) are developed to define shale gas extraction processes through dynamic porosity and permeability models of each component in different domains so that the complexities of interactions between different domains and among multiple physics can be deeply understood. Explicit fracture modelling and multi-continuum modelling methods are combined to achieve this. Particularly, both SRD and NSRD are characterized as dual-porosity-dual-permeability domains to reflect the heterogeneity of the shale. The SRD can be either continuous or discontinuous in geometry, where multiple properties differ from those in the NSRD to comprehensively reflect the stimulation effect of hydraulic fracturing on the shale matrix. This hybrid model is then validated against two previously published analytical models. It is also verified by comparing the simulation results against two sets of gas extraction data from the field. Based on sensitivity analysis, the multi-domain effects in mass transfer and mechanical deformation during shale gas production are investigated and discussed.

2. Conceptual model

In this section, a conceptual model is introduced to define the multiple physical processes in different porous media and domains in a shale gas reservoir, as well as the mass transfer and mechanical coupling relations between them. Especially, SRD and NSRD are defined based on the different rock properties of the IM in different regions to reflect the stimulation effect of hydraulic fracturing on the shale reservoir, and a 5-stage sequential flow conception is used to describe the sequence of gas transport.

2.1. Multi-scale model and domain division

A typical stimulated shale gas reservoir composed of three porous media (HF, IM and kerogen) distributed in three domains (HF, SRD and NSRD) is illustrated in Fig. 2. To incorporate the heterogeneity and
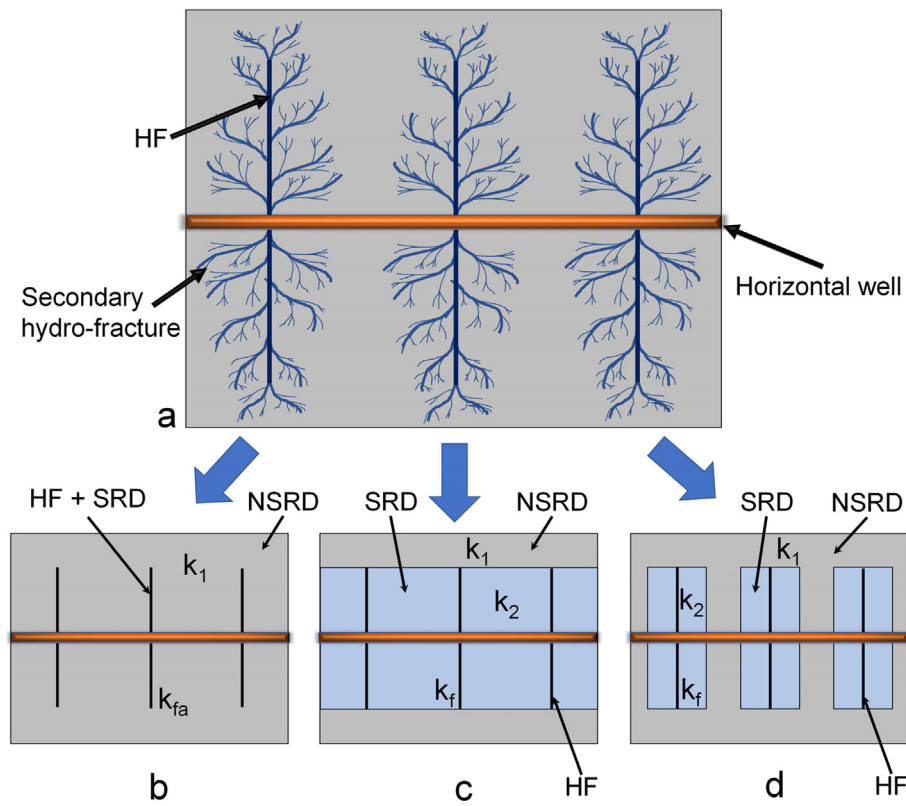
Fig. 1. Different methods of simplifying the SRD in shale reservoirs. (a) An hydraulically fractured shale reservoir with HFs and secondary hydro-fractures; (b) Method 1: Virtual 1-D fractures with an abstract permeability (k_{fa}), representing HFs + SRD [24]; (c) Method 2: HFs with a permeability of k_f + A continuous SRD with a permeability of k_2 [23]; (d) Method 3: HFs + A series of separated sub-SRDs [25]. k_1 is the permeability of the NSRD.
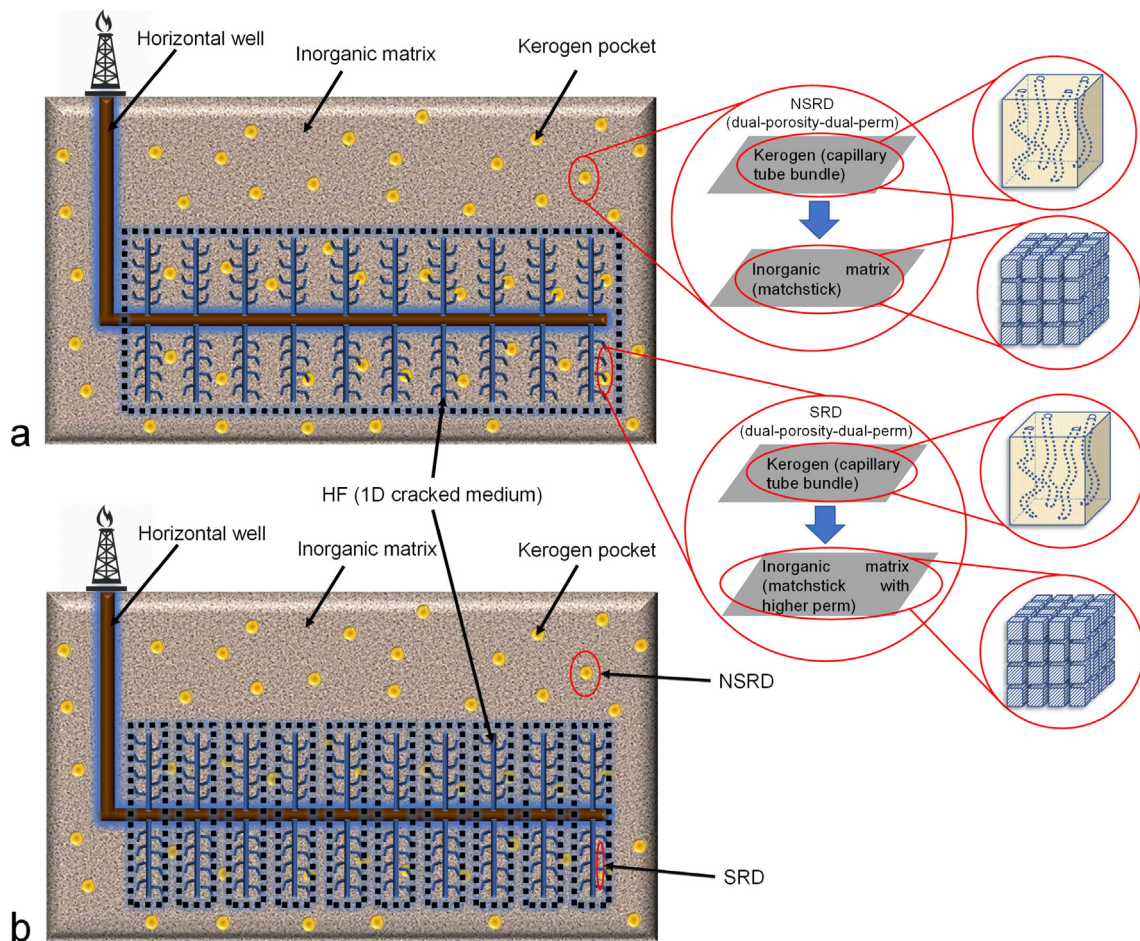

Fig. 2. Shale gas reservoir with multiple porous media and domains. (a) With a continuous SRD; (b) With a discontinuous SRD.

multi-domain characteristics of the shale reservoir, a multi-scale model with multiple domains is proposed as follows: (1) the NSRD is a continuous domain having all the original properties of shale. It is defined as a dual-porosity-dual-permeability system combining two overlapping porous continua: kerogen and IM. That is, kerogen and IM have different pressure systems interacting with each other. More specifically, kerogen is conceptualized as a bundle of tortuous nanotubes holding both free gas and adsorbed gas [32], while IM is simplified to a bundle of prismatic matchsticks. Free gas in the IM flows through the slot-shape natural fractures, which is analogous to a coal seam with cleats [34] except that the weak sorption effect in the IM is neglected [18,35,36]. (2) Similarly, the SRD is also simplified as an overlapping assembly of kerogen and IM, whereas its initial porosity, permeability and compressibility in the IM are different from those in the NSRD. Another difference from the NSRD is that, the SRD geometry is explicitly specified based on the study of Stalgorova and Mattar [25]. Thus, the SRD can be either continuous [Fig. 2(a)] or discontinuous [Fig. 2(b)] depending on the efficiency of hydraulic fracking treatment. (3) The HF is simplified as a 1-D inorganic cracked medium [24].

2.2. Sequence of gas transport in multiple domains

A sequential process is summarized to depict gas transport in the shale reservoir as illustrated in Fig. 3 [11,24]: At the initiation of gas extraction, gas in the HF rapidly flows out due to the difference between the bottom-hole pressure and initial reservoir pressure. Over a short period, gas pressure in the HFs become much lower than that in the shale matrix (Stage 1), inducing the free gas in the IM of the SRD to flow into the HFs (Stage 2). The decreased pressure in the IM then makes the kerogen in the SRD start to supply gas in the forms of free gas and desorbed gas (Stage 3). After that, due to the differential pressure between SRD and NSRD, gas in the IM in the NSRD gradually flows into the IM in the SRD (Stage 4). Finally, gas in kerogen in the NSRD begins flowing into IM in the NSRD. Previously, the sequence of Stages 1–3 has been demonstrated by Peng et al. (2015) [11] to be capable of reflecting the gas transport behaviour in shale gas reservoirs, but the SRD and NSRD are not differentiated in their study. Here, we further extend the sequence to 5-stages so that gas transport in the SRD and the NSRD with different properties in a hydraulic fractured reservoir can be considered separately.

2.3. Multiple physics in shale gas production

As mentioned previously, three physical processes influencing shale gas extraction should be considered in modelling: Above all, each medium in each domain is influenced by the varying effective stress. Therefore, a stress–strain constitutive relationship is needed to couple the deformation of the entire reservoir [29]. In addition, gas desorption occurs in kerogen, resulting in three effects including gas supply (described by the mass transfer equation in kerogen), sorption-induced volumetric strain (as a contribution to the whole mechanical coupling relationship) and the volumetric effect of the adsorbed gas layer (as a contribution to the change of kerogen porosity). Thirdly, flow regimes in kerogen and IM may be slip flow or transition flow due to the extremely small pore size, while gas flow in the HF is deemed as continuum flow following Darcy's law due to the relatively large HF aperture [12,24]. It should be noted that flow regime effects in the IM differ in SRD and NSRD because the IM has different pore sizes in these two domains. The applied scope of these mechanisms are also marked in Fig. 3. In the following section, the mathematical model is detailed based on the conceptual model.

3. Model formulation

In this section, a mechanical equation is first given to fully couple the stress-deformation relationship for the entire shale formation. After that, the equations describing gas transport in each porous medium and domain, and the mass exchange between them are derived. As two core properties, effective porosity and apparent permeability are defined to incorporate the effects of various physical processes [37]. All the equations in this section are derived based on the following assumptions: (1) Both kerogen and IM are isotropic and linear-elastic continua; (2) The reservoir is saturated by methane; (3) The effect of water in the shale is ignored; (4) Strains are infinitesmimal; and (5) Gas extraction is an isothermal process.

3.1. Mechanical coupling equations

We begin with the stress – strain relationship of the entire shale reservoir based on the Biot's theory of poroelasticity and the dual-porosity assumption [11,24,38,39]:
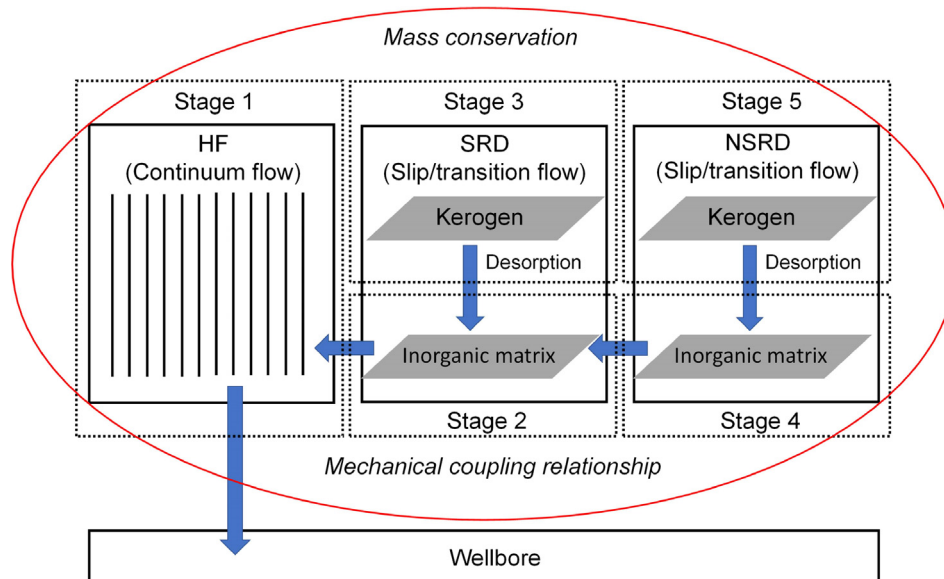

Fig. 3. Gas transport sequence and mechanisms in a hydraulically fractured shale reservoir.

$$\varepsilon_{ij} = \frac{1}{2G}\sigma_{ij} - \left(\frac{1}{6G} - \frac{1}{9K}\right)\sigma_{KK}\delta_{ij} + \frac{\alpha_k p_k}{3K}\delta_{ij} + \frac{\alpha_m p_m}{3K}\delta_{ij} + \frac{\varepsilon_s}{3}\delta_{ij} \tag{1}$$

where ε_{ij} is the component of the total strain tensor; G is the bulk shear modulus of shale; K is the bulk volumetric modulus of shale; $\sigma_{KK} = \sigma_{11} + \sigma_{22} + \sigma_{33}$; σ_{11}, σ_{22} and σ_{33} are the normal stresses in the three axis directions of the spatial coordinate system, respectively; δ_{ij} is the Kronecker delta; ε_s is the sorption-induced volumetric strain; p_k and p_m are the pressures of kerogen and IM, respectively; α_k is the effective Biot coefficient of kerogen and α_m is the effective Biot coefficient of IM. α_k and α_m reflect the contributions of kerogen and IM to the fluid volume change induced by bulk volume changes in the drained condition [38,40]. They are defined according to the studies of Mehrabian and Abousleiman (2015) [41] and Cao et al. (2016) [24]:

$$\begin{cases} \alpha_k = \frac{\gamma_k K \bar{\alpha_k}}{K_k} \\ \alpha_m = \frac{\gamma_m K \bar{\alpha_m}}{K_m} \end{cases} \tag{2}$$

where K denotes the bulk volumetric modulus of shale; γ_k and γ_m are the volumetric fractions occupied by kerogen and IM, respectively, $\gamma_k + \gamma_m = 1$. $\bar{\alpha_k}$ and $\bar{\alpha_m}$ are the individual Biot coefficients of kerogen and IM, respectively. They are defined by the following expressions:

$$\begin{cases} \bar{\alpha_k} = 1 - \frac{K_k}{K_{ks}} \\ \bar{\alpha_m} = 1 - \frac{K_m}{K_{ms}} \end{cases} \tag{3}$$

where K_k is the bulk modulus of kerogen; K_m is the bulk modulus of IM; K_{ks} is the bulk modulus of solid particles of kerogen; K_{ms} is the bulk modulus of solid particles of IM. Substituting Eq. (3) into Eq. (2) yields the following expressions:

$$\begin{cases} \alpha_k = \frac{\gamma_k K}{K_k}\left(1 - \frac{K_k}{K_{ks}}\right) = \gamma_k\left(\frac{K}{K_k} - \frac{K}{K_{ks}}\right) \\ \alpha_m = \frac{\gamma_m K}{K_m}\left(1 - \frac{K_m}{K_{ms}}\right) = \gamma_m\left(\frac{K}{K_m} - \frac{K}{K_{ms}}\right) \end{cases} \tag{4}$$

Apparent from Eq. (4) is that α_k and α_m are determined from γ_k, γ_m, K, K_k, K_m, K_{ks} and K_{ms}. These parameters can be obtained from core analysis [42] and mechanical tests [43,44]. Another approach to obtain α_k and α_m is, firstly determining $\bar{\alpha_k}$ and $\bar{\alpha_m}$ by acoustic measurements [42,45], and then calculating α_k and α_m from Eq. (2).

Note that K in Eq. (1) is a volumetric-weighted quantity expressed as the follow [24,40]:

$$\frac{1}{K} = \frac{\gamma_k}{K_k} + \frac{\gamma_m}{K_m} \tag{5}$$

Additionally, ε_s can be expressed as the following Langmuir-type formula [7,39]:

$$\varepsilon_s = \frac{\varepsilon_L p_k}{p_k + P_L} \tag{6}$$

where ε_L and P_L are the Langmuir sorption strain and Langmuir pressure constants of shale. Note that the adsorption-induced strain is negligible in IM, while significant in kerogen.

On the right-hand-side of Eq. (1), the first and second terms denote the strains induced by the stress tensor in the normal- and shear- directions, respectively; the third and fourth terms are the strains caused by the gas pressure in kerogen and IM, respectively; and the final term is the contribution of sorption-induced strain on the total strain tensor.

Furthermore, the strain tensor ε_i can also be expressed as displacements [38,39]:

$$\varepsilon_i = \frac{1}{2}(u_{i,j} + u_{j,i}) \tag{7}$$

where $u_{i,j}$ represents the first-order partial derivative of displacement. The force equilibrium equation neglecting inertial effects is given as:

$$\sigma_i + f_{,i} = 0 \tag{8}$$

where σ_i is the total stress tensor and $f_{,i}$ is the partial derivative of the body force.

Combining Eqs. (1), (6), (7) and (8) yields the Navier-type equation as the final mechanical constitutive relationship:

$$\frac{3K(1-2\upsilon)}{2(1+\upsilon)}u_{i,kk} + \frac{3K}{2(1+\upsilon)}u_{k,ki} - \alpha_k p_{k,i} - \alpha_m p_{m,i} - \frac{K\varepsilon_L P_L}{(p_k + P_L)^2}p_{k,i} + f_i$$
$$= 0 \tag{9}$$

where υ is the bulk Possion's ratio of reservoir. Eq. (9) has a strict mathematical form to fully couple the mechanical deformation and the effect of pore pressures in kerogen and IM, and sorption-induced strain. The properties K, υ, and P_L can be obtained experimentally.

3.2. Gas transport in kerogen

3.2.1. Governing equation in kerogen

Based on mass conservation, the general governing equation for gas storage and flow in kerogen can be written as [24]:

$$\frac{\partial m_k}{\partial t} + \nabla \cdot \left(-\rho_{gk}\frac{k_{kapp}}{\mu_k}\nabla p_k\right) = -Q_{k-m} \tag{10}$$

where m_k is the mass storage term of gas in kerogen; ρ_{gk} is the gas density in kerogen; k_{kapp} is the apparent permeability of kerogen and $-Q_{k-m}$ is the mass sink term (providing mass for the IM system from kerogen). μ_k is the gas viscosity in kerogen. The general formulae for calculating gas density and viscosity in different porous media are given in **Appendix A**.

The storage term m_k can be further expressed as the mass sum of free gas and adsorbed gas:

$$m_k = \rho_{gk}\phi_{k,stress,ads} + \rho_a\rho_s V_{ads} \tag{11}$$

where $\phi_{k,stress,ads}$ is the effective kerogen porosity considering stress dependence and volumetric effect of the adsorbed gas layer; ρ_a is the gas density under standard conditions, 0.717 kg/m^3 [39]; ρ_s is the shale density; V_{ads} is the adsorption volume per unit of shale mass as standard gas volume. Numerous experimental investigations have demonstrated that V_{ads} for shale can be approximately calculated by the Langmuir isotherm [46,47,48]:

$$V_{ads} = \frac{V_L p_k}{P_L + p_k} \tag{12}$$

where V_L is the Langmuir volume constant of shale. Thus, the key issue of determining Eq. (10) is to derive the expressions for $\phi_{k,stress,ads}$, k_{kapp} and Q_{k-m} which are all influenced by the multiple physics in the producing shale reservoir.

To elucidate the effective porosity and apparent permeability models incorporating multiple effects, a schematic illustrating the various mechanisms of gas transport in kerogen is shown in Fig. 4. Under the initial condition, kerogen has the initial gas pressure p_{k0}, initial porosity ϕ_{k0}, initial effective pore radius r_{k0} and initial permeability k_{k0}, as shown in Fig. 4(a). Note that at the beginning of gas production, multiple effects including rock deformation, adsorption and flow regime are all present in the kerogen. Therefore, ϕ_{k0}, r_{k0} and k_{k0} are the results of interactions between the initial condition and kerogen with multiple physical effects. Another point is that, in the initial state, adsorbed gas has occupied some pore space, which is expressed as $\phi_{adsocc0}$. With gas pressure in the kerogen dropping from the initial value p_{k0} to p_k, the effects of deformation, adsorption and impact flow regime change as considered by the following: (1) Change in deformation. The decreased pore pressure leads to a change in deformation, resulting in changes in the stress-dependent porosity $\phi_{k,stress}$, pore radius $r_{k,stress}$ and permeability $k_{k,stress}$ [see the narrowed capillary in Fig. 4(b)]. (2) Change in volumetric effect of adsorbed gas layer. The pore volume initially partly occupied by the adsorbed gas layer changes from $\phi_{adsocc0}$ to ϕ_{adsocc} as a result of pressure-drop-induced desorption,
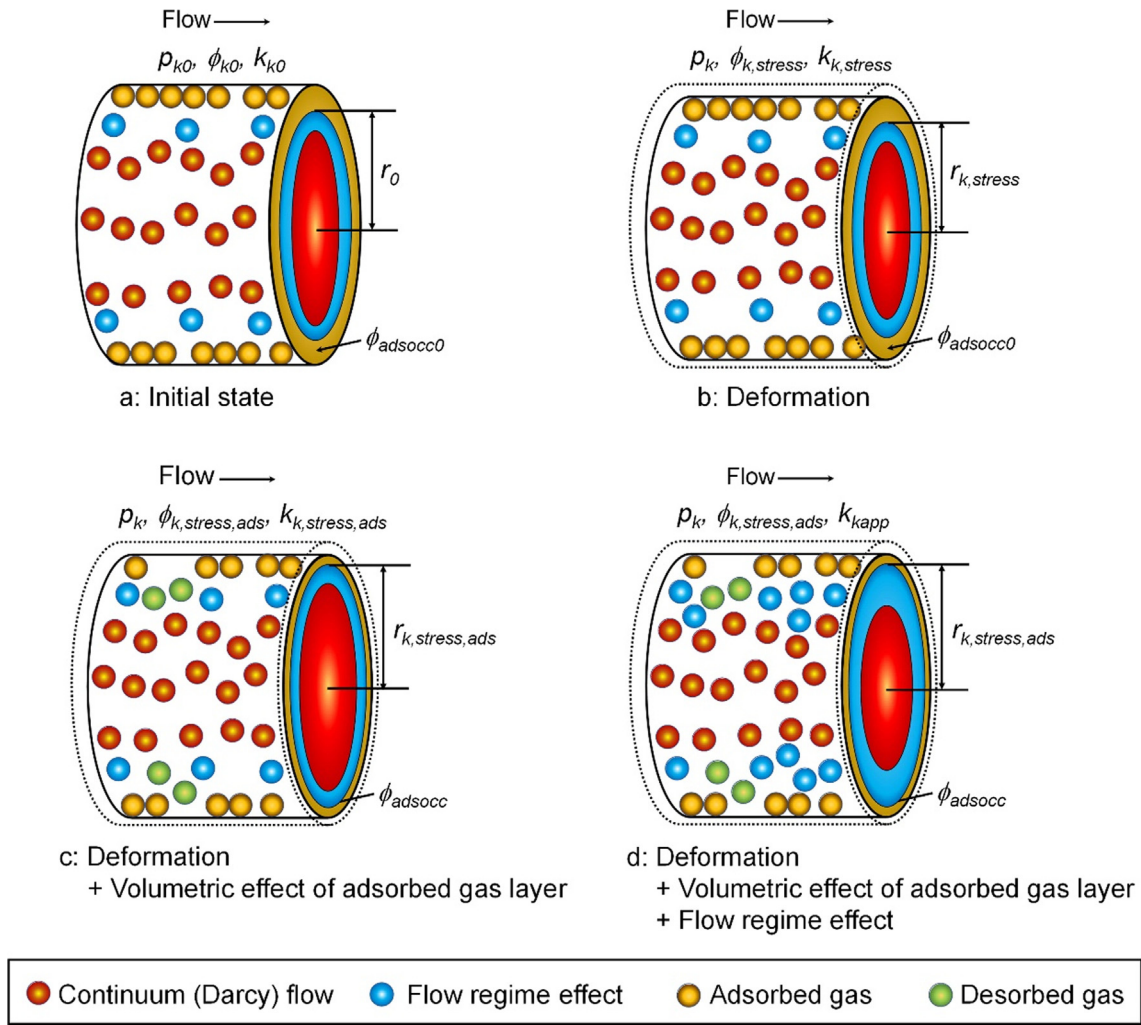
Fig. 4. Schematic of gas transport in kerogen. (a) A kerogen pore under the initial reservoir condition (p_k) with the effects of initial geo-stress and the initial adsorbed gas layer; (b) A producing kerogen pore (pore pressure = p_k), considering the change of deformation; (c) A producing kerogen pore (pore pressure = p_k), considering the changes of deformation + volumetric effect of adsorbed gas layer; (d) A producing kerogen pore (pore pressure = p_k), considering the changes of deformation + volumetric effect of adsorbed gas layer + flow regime effect.

resulting in changes in the effective porosity $\phi_{k,stress,ads}$, effective pore radius $r_{k,stress,ads}$ and the stress-desorption-dependent permeability $k_{k,stress,ads}$ [see the capillary with decreased adsorbed gas in Fig. 4(c)]. Meanwhile, some initially adsorbed gas molecules desorb and supply the free-gas flow. (3) Change in flow regime effect. The flow regime effect in extremely small pores (blue spheres – Fig. 4) enhances the flow compared to the classic continuum flow (red spheres – Fig. 4). This enhancing effect, varies with the change oin pore pressure and effective radius during gas production, resulting in the dynamic change in apparent permeability of kerogen k_{kapp} [see the capillary with increased blue spheres in Fig. 4(d)]. Therefore, considering the three effects mentioned, the expressions of $\phi_{k,stress,ads}$, $r_{k,stress,ads}$ and k_{kapp} should be derived to conduct the simulation of gas transport in kerogen. Given the known initial properties of kerogen, we achieve this objective as described in the following sections through a step-by-step method: (1) Considering the change of effective stress (Section 3.2.2); (2) Considering the volumetric change of the adsorbed gas layer (Section 3.2.3); (3) Considering the change of flow regime effect (Section 3.2.4).

3.2.2. Stress dependence in kerogen

A porosity model, proposed by Cui and Bustin [49], and based on mean effective stress change is selected to incorporate stress dependence. It has been demonstrated valid for shale formations [24,50]. For a deformable porous medium under geo-stress, the porosity increment $d\phi$ caused by changing pore pressure dp can be expressed as:

$$\frac{d\phi}{\phi} = C(d\bar{\sigma} - dp) \tag{13}$$

where $C = \alpha/(\phi_0 \cdot K)$ denotes the bulk compressibility of the porous medium [49,51], α is the Biot coefficient of the porous medium, ϕ_0 is the initial porosity and K is the bulk modulus. $\bar{\sigma}$ is the mean total stress and p is the pore pressure. Note that Eq. (13) can be applied to various porous media without the restriction of pore shape. The reason is that, the porosity variation in this equation is controlled by the changes of mean total stress and pore pressure, and these two controlling factors are both averaged physical quantities (i.e., this model is independent of pore shape). Applying Eq. (13) to kerogen and integrating this equation yields the following equation to determine the stress-independent porosity of the kerogen ($\phi_{k,stress}$):

$$\phi_{k,stress} = \phi_{k0} \exp\{-C_k[(\bar{\sigma} - \bar{\sigma}_0) - (p_k - p_{k0})]\} \tag{14}$$

where $-\sigma-\sigma_0$ is the initial mean total stress; p_{k0} is the initial pore pressure in kerogen; $C_k = \alpha_k/(\phi_{k0} \cdot K_k)$ denotes the bulk compressibility of kerogen [49,51]. According to the cubic law [34]:

$$\frac{k_{k,stress}}{k_{k0}} = \left(\frac{\phi_{k,stress}}{\phi_{k0}}\right)^3 \qquad (15)$$

where $k_{k,stress}$ is the permeability of kerogen influenced by geo-stress. Combining Eqs. (14) and (15), $k_{k,stress}$ can be expressed as:

$$k_{k,stress} = k_{k0}\exp\{-3C_k[(\bar{\sigma} - \bar{\sigma}_0) - (p_k - p_{k0})]\} \qquad (16)$$

The next issue is to determine the expression for $r_{k,stress}$ because it is related to the flow regime effect in kerogen. First of all, applying the Hagen-Poiseuille equation for a bundle of capillaries to nanopores in kerogen, the initial pore radius r_{k0} has the following expression [26,33,52]:

$$r_{k0} = \sqrt{\frac{8k_{k0}\tau_{k0}}{\phi_{k0}}} \qquad (17)$$

where τ_{k0} is the initial tortuosity of kerogen as a function of ϕ_{k0} [53]:

$$\tau_{k0} = \frac{1}{\phi_{k0}^{q_k}} \qquad (18)$$

where q_k is the Archie cementation index which can be experimentally obtained [54]. Similarly, the $r_{k,stress}$ and the stress-dependent tortuosity of kerogen $\tau_{k,stress}$ at a certain stress state can be expressed as:

$$r_{k,stress} = \sqrt{\frac{8k_{k,stress}\tau_{k,stress}}{\phi_{k,stress}}} \qquad (19)$$

$$\tau_{k,stress} = \frac{1}{\phi_{k,stress}^{q_k}} \qquad (20)$$

Combining Eqs. (15), (17), (18), (19) and (20) gives

$$r_{k,stress} = r_{k0}\cdot\left(\frac{\phi_{k,stress}}{\phi_{k0}}\right)^{1-0.5q_k} \qquad (21)$$

$$\tau_{k,stress} = \tau_{k0}\cdot\left(\frac{\phi_{k0}}{\phi_{k,stress}}\right)^{q_k} \qquad (22)$$

Thus, Eqs. (14), (16), (21) and (22) and reflect the effects of stress on the permeability, porosity, pore radius and tortuosity of kerogen. We also see that porosity is the key factor linking these equations since all other quantities relate to the change in porosity.

3.2.3. Volumetric effect of adsorbed gas layer in kerogen

We further consider the volumetric change of the adsorbed gas layer based on $\phi_{k,stress}$. Based on the comparison of Fig. 4(b) and (c), the kerogen porosity, influenced by both stress and adsorbed gas layer $\phi_{k,stress,ads}$ with p_k, can be expressed as:

$$\phi_{k,stress,ads} = \phi_{k,stress} + \phi_{adsocc0} - \phi_{adsocc} = \phi_{k,stress} - \Delta\phi_{adsocc} \qquad (23)$$

where $\phi_{adsocc0}$ is the porosity occupied by the adsorbed gas layer at the initial state (p_{k0}); ϕ_{adsocc} is the porosity occupied by the adsorbed gas layer with p_k; $\Delta\phi_{adsocc} = \phi_{adsocc} - \phi_{adsocc0}$ is the change in porosity occupied by the gas adsorption layer. $\phi_{adsocc0}$ and ϕ_{adsocc} can be readily determined based on the Langmuir adsorption isotherm [Eq. (12)]:

$$\begin{cases} \phi_{adsocc0} = \frac{\rho_a\rho_{sk}V_{ads0}}{\rho_{kads0}} = \frac{\rho_a\rho_{sk}V_Lp_{k0}}{\rho_{kads0}(P_L + p_{k0})} \\ \phi_{adsocc} = \frac{\rho_a\rho_{sk}V_{ads}}{\rho_{kads}} = \frac{\rho_a\rho_{sk}V_Lp_k}{\rho_{kads0}(P_L + p_k)} \end{cases} \qquad (24)$$

where V_{ads0} is the initial adsorbed volume per unit mass of shale calculated from Eq. (12); ρ_{sk} is the kerogen density; ρ_{kads} is the adsorbed gas density which is a function of p_k; and ρ_{kads0} is the initial adsorbed gas density. According to the study conducted by Riewchotisakul and Akkutlu [55], this function can be represented as a logarithm as:

$$\rho_{kads} = a\ln p_k + b \qquad (25)$$

where a and b are fitting coefficients related to temperature. For

instance, at 353 K, $a = 105.7$ and $b = 1397.13$ [55]. This equation indicates that the adsorbed gas density decreases with depressurization. This equation is equivalent to Eq. (21) in their original manuscript.

By applying the cubic law again, $k_{k,stress,ads}$ can be given as:

$$k_{k,stress,ads} = k_{k,stress}\cdot\left(\frac{\phi_{k,stress,ads}}{\phi_{k,stress}}\right)^3 \qquad (26)$$

Based on the analogy of Eqs. (21) and (22), the tortuosity and radius of kerogen considering stress and adsorbed gas layer can be expressed as:

$$r_{k,stress,ads} = r_{k,stress}\cdot\left(\frac{\phi_{k,stress,ads}}{\phi_{k,stress}}\right)^{1-0.5q_k} \qquad (27)$$

$$\tau_{k,stress,ads} = \tau_{k,stress}\cdot\left(\frac{\phi_{k,stress,ads}}{\phi_{k,stress}}\right)^{q_k} \qquad (28)$$

where $\tau_{k,stress,ads}$ is the kerogen tortuosity influenced by both stress and adsorbed gas layer. Hence, Eqs. (23), (26)–(28) reflect the volumetric effect of adsorbed gas layer on the permeability, porosity, pore radius and tortuosity of kerogen.

3.2.4. Flow regime effect in kerogen

Knudsen number Kn is a quantity related to the collision between gas molecules and that between gas molecules and the skeleton of the porous medium, which determines the regime of gas flow. Based on the value of Kn, gas flow in shale can be categorized into four regimes including: (1) Continuum flow ($Kn \leq 0.001$); (2) Slip flow ($0.001 < Kn \leq 0.1$); (3) Transition flow ($0.1 < Kn \leq 10$) and (4) Molecular flow ($Kn > 10$). Each of the last three regimes leads to an enhanced apparent permeability compared to the permeability for continuum flow (based on Darcy's law). A general method for calculating Kn in different domains of shale is given in **Appendix B**. A permeability enhancement function $f_k(Kn_k)$ generalizes the effect of the flow regime according to the studies performed by Beskok and Karniadakis [56]; Civan [32]; and Civan et al. [57]. Thus, the apparent permeability of kerogen k_{kapp} can be expressed as:

$$\begin{cases} k_{kapp} = k_{k,stress,ads}\cdot\frac{f_k(Kn_k)}{f_k(Kn_{k0})} \\ f_k(Kn_k) = (1 + \zeta_k Kn_k)\left(1 + \frac{4Kn_k}{1 + Kn_k}\right) \end{cases} \qquad (29)$$

where Kn_{k0} is the initial Knudsen number in kerogen. ζ_k is the rarefaction coefficient in kerogen calculated by the following empirical formula:

$$\zeta_k = \frac{\zeta_0}{1 + \frac{A}{Kn_k^B}} \qquad (30)$$

where ζ_0 is an asymptotic limit value; A and B are empirical coefficients. For an ultra-low permeability gas reservoir, $A = 0.178$; $B = 0.4348$; $\zeta_0 = 1.358$ [32]. These empirical coefficients have been shown valid for shale formations in many previous studies [57,58,24]. Eq. (29) reflects the flow regime effect and gives the final expression of apparent permeability of kerogen. Note that a kind of "surface diffusion" may occur on the adsorbed gas layer of kerogen. However, many previous investigations have suggested that this transport is negligible during practical shale gas extraction in most cases, and provides an obvious contribution to gas transport only under very low pressure [12,59,60]. Hence, surface diffusion in kerogen is ignored here.

3.2.5. Sink term

With the depletion of reservoir pressure, the free gas in kerogen flows to IM under the driving differential pressure between these two porous media – this is the sink term. Accord to the inter-media mass transfer theory proposed by Kazemi et al. (1992) [61], we have:

$$Q_{k-m} = \frac{D_{k-m}\rho_{gk}k_{kapp}}{\mu_k}(p_k - p_m) \tag{31}$$

where D_{k-m} is a shape factor related to specific interfacial area of the kerogen pockets. For uniform spherical kerogen pockets, $D_{k-m} = 3/R^2$, where R is the mean radius of the spherical kerogen pockets. Combining Eqs. (10), (11), (16), (23), (29) and (31) gives the overall governing equation for kerogen:

$$\begin{cases} \frac{\partial(\rho_{gk}\phi_{k,stress,ads} + \rho_a\rho_s V_{ads})}{\partial t} + \nabla\cdot\left(-\rho_{gk}\frac{k_{kapp}}{\mu}\nabla p_k\right) = -\frac{D_{k-m}\rho_{gk}k_{kapp}}{\mu_k}(p_k - p_m) \\ k_{kapp} = k_{k0}\exp\{-3C_k[(\bar{\sigma} - \bar{\sigma}_0) - (p_k - p_{k0})]\}\cdot\left(\frac{\phi_{k,stress,ads}}{\phi_{k,stress}}\right)^3\cdot\frac{f_k(Kn_k)}{f_k(Kn_{k0})} \end{cases} \tag{32}$$

3.3. Gas transport in inorganic matrix

3.3.1. Governing equation in inorganic matrix

The governing equation for the IM takes a similar form to that of kerogen except for the following differences: (1) Desorption is not considered; (2) The shape of the inorganic pores are prescribed as slots instead of circular capillaries; (3) The IM has two domains, i.e., SRD and NSRD with different properties. These two domains exchange gas mass through a boundary condition; (4) IM receives gas from kerogen while giving gas to the HFs.

The governing equation in the IM for SRD and NSRD can be expressed as:

$$\frac{\partial(\rho_{gm}^j\phi_{m,stress}^j)}{\partial t} + \nabla\cdot\left(-\rho_{gm}^j\frac{k_{mapp}^j}{\mu_m^j}\nabla p_m^j\right) = Q_{k-m}^j \tag{33}$$

where the superscript j is a domain indicator, j = SRD or NSRD; ρ_{gm} and μ_m denote the gas density and viscosity in the IM, respectively; $\phi_{m,stress}$ is the IM porosity influenced by stress; k_{mapp} is the apparent permeability of IM and Q_{k-m}^j is the mass source term (providing gas for the IM system from kerogen) in domain j. Note that the basic rock properties of the SRD and NSRD in a stimulated shale reservoir are different, which will be further discussed in Section 4.

3.3.2. Stress dependence in inorganic matrix

Considering stress dependence, applying the Cui and Bustin model [47] to IM, $\phi_{m,stress}$ and $k_{m,stress}$ can be expressed as [24,50]:

$$\begin{cases} \phi_{m,stress}^j = \phi_{m0}^j\exp\{-C_m^j[(\bar{\sigma}^j - \bar{\sigma}_0^j) - (p_m^j - p_{m0}^j)]\} \\ k_{m,stress}^j = k_{m0}^j\exp\{-3C_m^j[(\bar{\sigma}^j - \bar{\sigma}_0^j) - (p_m^j - p_{m0}^j)]\} \end{cases} \tag{34}$$

where ϕ_{m0} and k_{m0} are the initial porosity and permeability of the IM, respectively; $C_m = \alpha_m/(\phi_{m0}\cdot K_m)$ denotes the bulk compressibility of the IM. Note that Eq. (34) has an analogous form to Eq. (14) due to the independence of Eq. (13) from pore shape. Similar to Section 3.2.2, the stress-dependent average aperture $b_{m,stress}$ and stress-dependent tortuosity $\tau_{m,stress}$ of fractures in the IM can be expressed as:

$$\begin{cases} b_{m,stress}^j = b_{m0}^j\cdot\left(\frac{\phi_{m,stress}^j}{\phi_{m0}^j}\right)^{1-0.5q_m} \\ \tau_{m,stress}^j = \tau_{m0}^j\cdot\left(\frac{\phi_{m0}^j}{\phi_{m,stress}^j}\right)^{q_m} \end{cases} \tag{35}$$

where b_{m0} and τ_{m0} are the initial aperture and initial tortuosity of fractures in the IM, respectively. τ_{m0} is a function of ϕ_{m0}:

$$\tau_{m0}^j = \frac{1}{(\phi_{m0}^j)^{q_m}} \tag{36}$$

where q_m is the Archie cementation index of IM.

3.3.3. Flow regime effect in inorganic matrix

The apparent permeability of the IM (k_{mapp}) can be expressed as:

$$k_{mapp}^j = k_{m,stress}^j\cdot\frac{f_m(Kn_m^j)}{f_m(Kn_{m0}^j)} \tag{37}$$

where $f_m(Kn_m)$ is the enhancement function for apparent permeability caused by the flow regime effect in IM. Kn_m is the Knudsen number in IM representing a certain pressure state and Kn_{m0} is the initial Knudsen number in the IM calculated by the formulas given in **Appendix B**. Note that the form of $f_m(Kn_m)$ is slightly different from that of $f_k(Kn_k)$ (having a coefficient of 6 instead of 4) due to the shape discrepancy between a circular tube (kerogen pores) and a rectangular slot (natural fractures of IM) [35]:

$$f_m(Kn_m^j) = (1 + \zeta_m Kn_m^j)\left(1 + \frac{6Kn_m^j}{1 + Kn_m^j}\right) \tag{38}$$

where ζ_m is the rarefaction coefficient in the IM:

$$\zeta_m = \frac{\zeta_0}{1 + \frac{A}{(Kn_m^j)^B}} \tag{39}$$

3.3.4. Boundary conditions for gas transport between different porous media and domains

At the boundary between SRD and NSRD, the pressure should be continuous as:

$$p_m^{NSRD}|_{at\ SRD\ boundary} = p_m^{SRD}|_{at\ SRD\ boundary} \tag{40}$$

Similarly, the mass flux should also be continuous at this boundary:

$$\overrightarrow{u_m^{NSRD}}|_{at\ SRD\ boundary} = \overrightarrow{u_m^{SRD}}|_{at\ SRD\ boundary} \tag{41}$$

where $\overrightarrow{u_m}$ denotes the mass flux in the IM. Meanwhile, continuity of both pore pressure and mass flux should also be satisfied for the HF which can be considered as an outlet boundary of IM:

$$p_m^{SRD}|_{at\ HF} = p_f|_{at\ HF} \tag{42}$$

$$\overrightarrow{u_m^{SRD}}|_{at\ HF} = \overrightarrow{u_f}|_{at\ HF} \tag{43}$$

where $\overrightarrow{u_f}$ is the inlet mass flux from SRD to HF; p_f is the gas pressure in HF.

Combining Eqs. (33), (34)-(43), we obtain the overall governing equation for the IM:

$$\begin{cases} \frac{\partial(\rho_{gm}^j\phi_{m,stress})}{\partial t} + \nabla\cdot\left(-\rho_{gm}^j\frac{k_{mapp}^j}{\mu_m^j}\nabla p_m^j\right) = \frac{D_{k-m}\rho_{gk}k_{kapp}}{\mu_k}(p_k - p_m) \\ k_{mapp} = k_{m0}\exp\{-3C_m[(\bar{\sigma} - \bar{\sigma}_0) - (p_m - p_{m0})]\}\cdot\frac{f_m(Kn_m^j)}{f_m(Kn_{m0}^j)} \\ p_m^{NSRD}|_{at\ SRD\ boundary} = p_m^{SRD}|_{at\ SRD\ boundary}\ ; \\ \overrightarrow{u_m^{NSRD}}|_{at\ SRD\ boundary} = \overrightarrow{u_m^{SRD}}|_{at\ SRD\ boundary} \\ p_m^{SRD}|_{at\ HF} = p_f|_{at\ HF}\ ; \quad \overrightarrow{u_m^{SRD}}|_{at\ HF} = \overrightarrow{u_f}|_{at\ HF} \end{cases} \tag{44}$$

Clearly, this equation is essential in representing gas production from a shale reservoir because it builds connections for mass transfer between kerogen, IM in SRD, IM in NSRD and HF by a source term and boundary conditions.

3.4. Gas transport in hydraulic fracture

Hydraulic fractures are conceptually simplified as a 1-D cracked medium at the outlet boundary of the IM. The stress dependence is considered here, while flow regime effect is ignored due to the relatively large aperture of the HF (millimetre-level). Desorption is also ignored. The governing equation is [7,11,24]:

$$\frac{\partial(\rho_{gf}\phi_{f,stress})}{\partial t} + \nabla_T \cdot \left(-b_{f,stress}\rho_{gf}\frac{k_{fapp}}{\mu_f}\nabla p_f\right) = 0 \tag{45}$$

where ∇_T denotes the gradient operator restricted to the tangential plane of the fracture; ρ_{gf} and μ_f are the gas density and viscosity in the HF, respectively; $\phi_{f,stress}$ and $b_{f,stress}$ are the HF porosity and aperture influenced by stress, respectively; k_{fapp} is the apparent permeability of the HF which is only affected by stress. Note that the inflow to the HF comes from the boundary flow in the SRD [see Eqs. (42) and (43)].

According to the definition of pore compressibility of the HF (C_f):

$$C_f = \frac{1}{\phi_{f,stress}}\frac{d\phi_{f,stress}}{dp_f} \tag{46}$$

Integrating this equation yields a simple expression for $\phi_{f,stress}$:

$$\phi_{f,stress} = \phi_{f0}\exp[C_f(p_f - p_{f0})] \tag{47}$$

where ϕ_{f0} is the initial porosity of the hydraulic fracture.

If the porosity change is small, the change ratio (the value of a quantity at a certain time point divided by its corresponding initial value) of the HF aperture can be approximately considered as equal to that of porosity [7,62]. Therefore, $b_{f,stress}$ can be expressed as:

$$b_{f,stress} = b_{f0}\cdot\frac{\phi_{f,stress}}{\phi_{f0}} = b_{f0}\exp[C_f(p_f - p_{f0})] \tag{48}$$

where b_{f0} is the initial aperture of HF.

For a slot-type fracture, the permeability can be expressed as $k_{f0} = b_{f0}^2/12$, where k_{f0} is the initial permeability of the HF, b_f is the aperture of the HF [62]. Similarly, $k_{fapp} = b_{f,stress}^2/12$, where k_{fapp} is the stress-dependent apparent permeability of the HF. Thus, k_{fapp} can be expressed as:

$$k_{fapp} = k_{f0}\cdot\left(\frac{b_{f,stress}}{b_{f0}}\right)^2 = k_{f0}\exp\{2C_f(p_f - p_{f0})\} \tag{49}$$

Both inflow and outflow of gas in the HF are controlled by boundary conditions. As apparent in Eqs. (42) and (43), the HF can be considered an outflow boundary of SRD, where the pore pressure and mass flux from IM in SRD are continuously inherited at this boundary. Meanwhile, the HF is also considered as a 1-D cracked porous medium in which the outlet pressure (at the intersection of HF and wellbore) is equal to the well bottom pressure (p_w). Therefore, the following boundary conditions should be satisfied:

$$\begin{cases} p_m^{SRD}|_{at\,HF} = p_f|_{at\,HF}; & \vec{u}_m^{SRD}|_{at\,HF} = \vec{u}_f|_{at\,HF} \\ p_f|_{at\,wellbore} = p_w \end{cases} \tag{50}$$

Combining Eqs. (33), (34), (37–43), we obtain the overall governing equation of HF:

$$\begin{cases} \frac{\partial(\rho_{gf}\phi_{f,stress})}{\partial t} + \nabla_T\cdot\left[-b_{f0}\rho_{gf}\exp[C_f(p_f-p_{f0})]\frac{k_{fapp}}{\mu_f}\nabla p_f\right] = 0 \\ k_{fapp} = k_{f0}\exp\{2C_f(p_f-p_{f0})\} \\ p_m^{SRD}|_{at\,HF} = p_f|_{at\,HF}; \quad \vec{u}_m^{SRD}|_{at\,HF} = \vec{u}_f|_{at\,HF} \\ p_f|_{at\,wellbore} = p_w \end{cases} \tag{51}$$

Eqs. (9), (32), (44) and (44) and constitute the multi-domain and multi-physics model for shale gas production fully coupled by mass transfer and mechanical deformation. The coupling relationship between these equations is summarized in Fig. 5. Compared to other existing numerical models for shale gas production, this proposed model has the following advantages: (1) SRD and NSRD are differentiated to reflect the property contrasts and the resultant difference in physical processes between these two domains; (2) A variety of mechanisms and effects are incorporated to describe the property evolution during gas production in the shale reservoir to ensure the accuracy of the
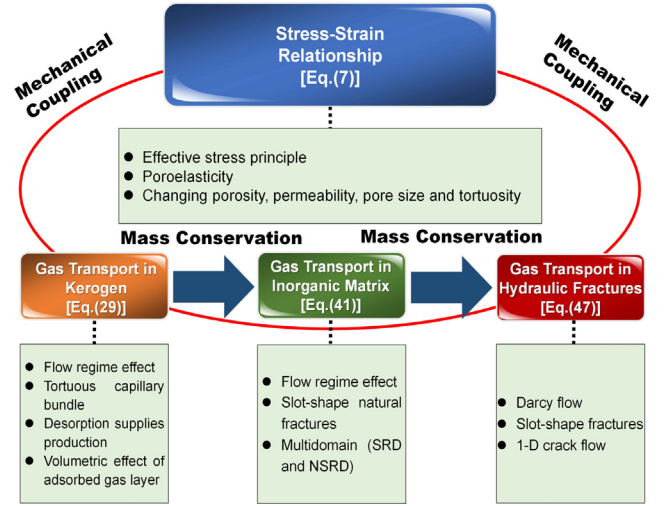

Fig. 5. Interaction and relationship between different media and domains in shale gas reservoir.

simulation.

4. Model validation and verification

Two sets of gas production data in shale gas plays in North America are obtained from the published literature to verify the proposed model. The fully coupled equations derived in Section 3 were implemented using COMSOL Multiphysics, a commercial PDE solver based on the finite element method (FEM). The HFs, as a series of 1-D cracked porous media, are explicitly specified in the geometry, while the IM and kerogen are simulated by the dual-continuum modelling method which gives coupled, superposed results of the equations for these two porous media at each node [9]. The first simulation case is for a producing reservoir in Marcellus Shale in North America. The computing parameters extracted from the literature are summarized in Table 1 [24,63]. The SRD and NSRD have different initial ϕ_{m0}, k_{m0}, C_m and IM Poisson's ratio (υ_m). Specifically, after fracking, new fractures are created, some of the natural fractures are activated, and the shale tends to be softer due to the soaking of the fracking fluid. Thus, $\phi_{m0}^{SRD} > \phi_{m0}^{NSRD}$, $k_{m0}^{SRD} > k_{m0}^{NSRD}$, $C_m^{SRD} < C_m^{NSRD}$ and $\upsilon_m^{SRD} > \upsilon_m^{NSRD}$. These changes can be obtained in advance by field logging or hydraulic fracturing modelling. The meshed geometry of a quarter of the reservoir (top view) and the boundary conditions are presented in Fig. 6(a). The reservoir is under a geo-stress field orthogonally decomposed as maximum and minimum horizontal geo-stresses (the overburden is considered as a constant). Gas flows under the driving force of differential pressure between the constant bottom-hole pressure and the initial reservoir pressure. Note that the SRD in this case is not continuous, but a set of separated sub-SRDs surrounding the individual HFs. More specifically, the single sub-SRD width (D_{SRD}) is equal to 15.24 m, which is half of the HF spacing for this simulation case. This value is back-calculated based on the simulation results. We first set some different D_{SRD}s to perform a series of preliminary simulations, and then determine a suitable D_{SRD} by comparing these results. We find that 15.24 m is a reasonable value for D_{SRD} which not only makes the simulation results match the field production data, but also holds the reservoir parameters close/identical to those in the literature [24,63]. It is apparent from Fig. 6(b) that during the 260-day production, the simulation results based on the proposed model (red line) have favorable agreement with the field data (symbols) except for the overestimated production in the first few days. This deviation is due to the hindrance of backflow of water in the early period of gas production, which is neglected in this study [24,64]. Also, the same case was calculated by using the classical tri-linear flow analytical model proposed by Brown et al. [23], as shown Fig. 6(b) (blue line).

Table 1

Reservoir and computational parameters for the Marcellus Shale case, used by the proposed numerical model and the analytical model proposed by Brown at al. [23,24,63,65,66].

Parameter (unit)	Proposed model	Analytical model	Literature value
Reservoir dimension (m × m × m)	1219.2 × 304.8 × 52.7	1219.2 × 304.8 × 52.7	1219.2 × 304.8 × 52.7
Geometric dimension (m × m × m)	609.6 × 152.4 × 52.7	609.6 × 152.4 × 52.7	609.6 × 152.4 × 52.7
Hydraulic fracture spacing (m)	30.5	30.5	30.5
Hydraulic fracture half-length (m)	85.3	85.3	85.3
Bottomhole pressure (Pa)	2.4×10^6	2.4×10^6	2.4×10^6
Reservoir temperature (K)	353	353	353
Number of hydraulic fractures	14	14	14
Horizontal well length (m)	426.7	426.7	426.7
Single sub-SRD width (m)	15.24	–	–
Gas viscosity (mPa·s)	Dynamically computed	2×10^{-5}	2×10^{-5}
Initial HF aperture (m)	0.003	0.03	0.003
Hydraulic fracture porosity	0.2	0.38	0.2
Initial HF permeability (m²)	3.0×10^{-14}	2.6×10^{-11}	3.0×10^{-14}
HF compressibility (Pa^{-1})	2.0×10^{-9}	9.43×10^{-8}	2.0×10^{-9}
Initial IM porosity	SRD: 0.06 NSRD: 0.03	0.03	0.03
Initial IM permeability (m²)	SRD: 5.0×10^{-19} NSRD: 1.0×10^{-19}	1.0×10^{-19}	1.0×10^{-19}
IM compressibility (Pa^{-1})	SRD: 3.0×10^{-10} NSRD: 4.5×10^{-10}	–	4.5×10^{-10}
Bulk modulus of matrix (Pa)	SRD: 2.0×10^{10} NSRD: 2.24×10^{10}	–	–
Volume fraction of kerogen	0.05	–	0.05
Kerogen pocket radius (m)	0.0005	–	0.0005
Initial kerogen porosity	0.1	–	0.01
Initial kerogen permeability (m²)	5.0×10^{-21}	–	5.0×10^{-21}
Kerogen compressibility (Pa^{-1})	1.16×10^{-10}	–	–
Possion's ratio	SRD: 0.25 NSRD: 0.2	–	0.2
Biot coefficient of IM	SRD: 0.45 NSRD: 0.38	–	–
Biot coefficient of kerogen	0.73	–	–
Langmuir pressure (MPa)	3.0	–	3.0
Langmuir volume (m³/kg)	2.5×10^{-3}	–	2.5×10^{-3}
Langmuir sorption strain constant	0.002	–	0.002
Maximum horizontal stress (MPa)	42.0	–	42.0
Minimum horizontal stress (MPa)	37.2	–	37.2
Shale density (kg/m³)	2460	–	–
Kerogen density (kg/m³)	2090	–	–
Archie cementation index of IM	2.5	–	–
Archie cementation index of kerogen	5	–	–
Compressibility of entire reservoir (Pa^{-1})	–	9.43×10^{-8}	–

The high consistency between the results of these two models and the field data demonstrate the validity of our model. It should be noted that, some of the key parameters used by the tri-linear flow model were adjusted to unrealistic values to match the field data (e.g., the HF permeability is 26,000 mD in contrast to 30 mD in the literature [24], see Table 1), while our numerical model used almost identical values in the literature. This indicates that our model performs better than the tri-linear flow analytical model in matching field data because we take
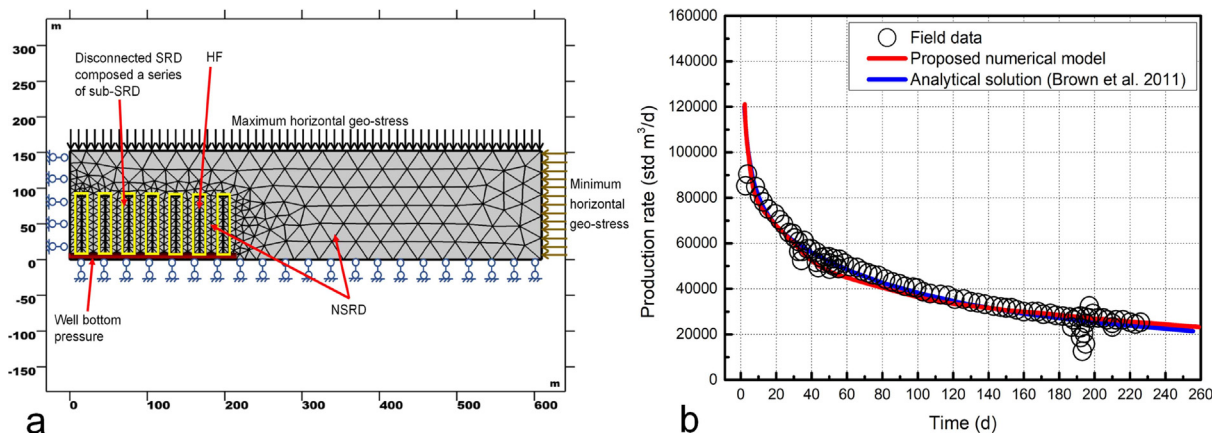
Fig. 6. Model validation and verification: Gas production in Marcellus Shale with a discontinuous SRD. (a) Top view of the meshed model geometry and boundary condition of a quarter-symmetry reservoir of Marcellus Shale with a discontinuous SRD; (b) Comparison among calculation results of the proposed model, tri-linear flow analytical model [23], and field data.
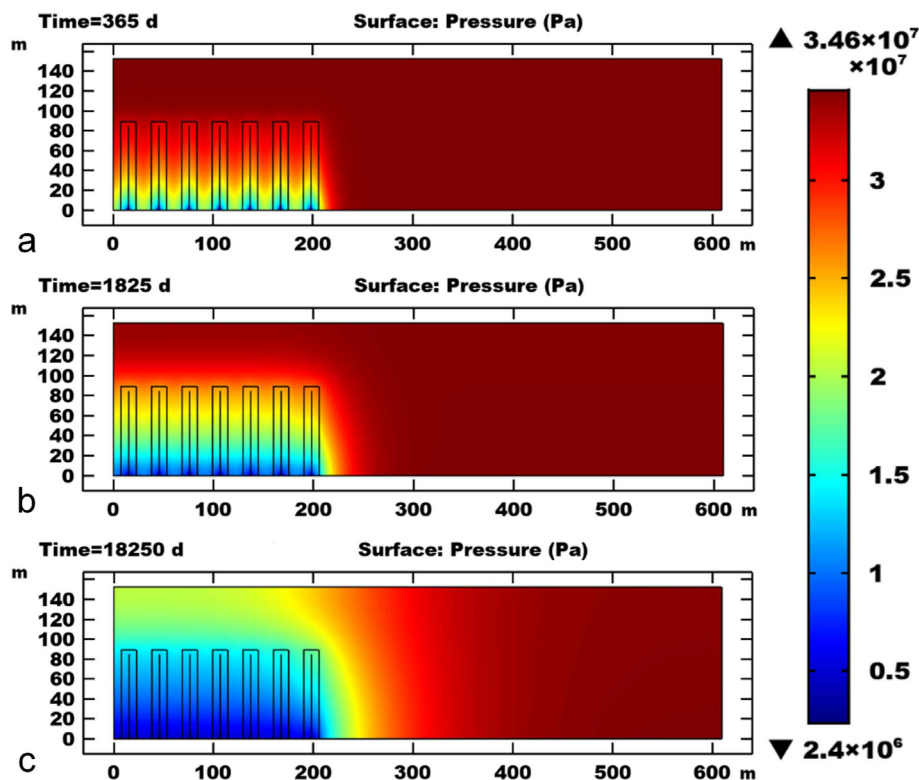
Fig. 7. Evolution of gas distribution in IM during production in Marcellus Shale, simulated using the proposed model after: (a) 1 year; (b) 5 years; (c) 50 years.

more factors into account to characterize real response. More specifically, matrix heterogeneity, stress dependence, flow regime effects, volumetric effects of the adsorbed gas layer and multi-domain characteristics are neglected in the tri-linear flow model [23]. Hence, incorporating additional mechanisms and features of real shale behaviour into the model is of importance in enhancing the accuracy of reservoir simulations.

We further simulated 50-year of production from the Marcellus Shale by using the proposed numerical model. The evolution of pressure distribution in IM is displayed in Fig. 7. It can be seen that the pressure rapidly depletes in the SRD near the HFs in the early stage of production, and the low-pressure zone spreads along the HF [Fig. 7(a)]. Meanwhile, pressure in the areas between these separated sub-SRDs also depletes quickly [Fig. 7(b)]. After 50-years of production, the SRD and the areas near the SRD have clearly lower pressures than the initial reservoir pressure, while the pressure in the NSRD far from the HFs also drops to some degree [Fig. 7(c)]. In addition, our simulation results suggest that pressure in the kerogen is always slightly higher than that in IM at the same location. Therefore, the pressure depletion process simulated in this case is consistent with the sequential flow process illustrated in Fig. 3, indicating the performance difference between domains. More details about this multi-domain effect will be discussed in Section 5.1.

As an example for a continuous SRD, the second simulation case represents a reservoir in Barnett Shale in the United States. Modeling parameters are obtained from the literature [10,24] and are listed in Table 2. Again, we mesh a one-quarter geometry with a continuous SRD and the boundary condition are illustrated in Fig. 8(a). Apparent from Fig. 8(b) is that the simulation results for 1600-days of production (the red line) closely match the field data (the dots). Furthermore, we also used an advanced analytical model proposed by Zeng et al. [67] to match these field data. This analytical model conceptually divides the shale gas reservoir into 7 linear-flow zones and uses very complex analytical equations to solve for gas flow rate. The results based on the analytical model [blue line in Fig. 8(b)] agree closely with those given

by the proposed numerical model, establishing the validity of our model. Compared to the analytical model proposed by Zeng et al. [67], which can only calculate mean pseudo-pressure instead of exact pressure distribution, and does not consider the mechanical factors, our numerical model incorporates the stress dependence in different domains and the volumetric effect of the adsorbed gas layer in kerogen. Another advantage of our model over Zeng's model is that the pressure distribution in the entire geometry can be readily evaluated at any time by using FEM. In summary, the proposed model in this work is demonstrated to be both valid and accurate in simulating gas production processes from various shale reservoirs with continuous/discontinuous SRDs.

5. Results and discussion

The proposed model provides insight into shale gas extraction because it comprehensively includes characteristics of shale reservoirs, mechanisms of gas transport in shale, and interactions between multiple media and domains. Here, we give some important simulation results and discussion to strengthen the understanding of mass transfer and mechanical deformation in different domains during shale gas production. All the results in this section are based on a sensitivity analysis of the simulation case for the Marcellus shale reservoir mentioned above.

5.1. Multi-domain effects in mass transfer

The basic property contrasts between HF, SRD and NSRD determine the different roles played by these domains in shale gas production. More specifically, HF, as the most permeable domain, provides necessary flow channels for gas flowing out of the tight shale, but it has very low gas storage due to its small total volume. The NSRD has the highest reserve due to its large volume, but it has an extremely low permeability. Moreover, NSRD does not contact the HF, implying a slow gas depletion process in the NSRD. As a result, the contribution of the HF to

Table 2

Reservoir and modeling parameters for the case of Barnett Shale, used in the proposed numerical model and the analytical model proposed by Zeng et al. [10,24,67,68,69].

Parameter (unit)	Proposed model	Analytical model	Literature value
Reservoir dimension (m × m × m)	1100 × 290 × 90	1100 × 290 × 90	1100 × 290 × 90
Geometric dimension (m × m × m)	550 × 145 × 90	550 × 145 × 90	550 × 145 × 90
Hydraulic fracture spacing (m)	30.5	30.5	30.5
Hydraulic fracture half-length (m)	47.2	47.2	47.2
Bottomhole pressure (Pa)	3.69×10^6	3.69×10^6	3.69×10^6
Reservoir temperature (K)	353	353	353
Number of hydraulic fractures	28	28	28
Horizontal well length (m)	853.4	853.4	853.4
Single sub-SRD width (m)	30.48	–	–
Gas viscosity (mPa·s)	Dynamically computed	2×10^{-5}	2×10^{-5}
Initial HF aperture (m)	0.003	0.03048	0.003
Hydraulic fracture porosity	0.2	0.38	0.2
Initial HF permeability (m²)	5.0×10^{-14}	1.7×10^{-14}	5.0×10^{-14}
HF compressibility (Pa^{-1})	2.0×10^{-9}	–	2.0×10^{-9}
Initial IM porosity	SRD: 0.065 NSRD: 0.03	0.03	0.03
Initial IM permeability (m²)	SRD: 1.0×10^{-18} NSRD: 2.0×10^{-19}	4.0×10^{-19}	2.0×10^{-19}
IM compressibility (Pa^{-1})	SRD: 3.1×10^{-10} NSRD: 4.5×10^{-10}	–	4.5×10^{-10}
Bulk modulus of matrix (Pa)	SRD: 2.26×10^{10} NSRD: 2.67×10^{10}	–	–
Volume fraction of kerogen	0.05	–	0.05
Kerogen pocket radius (m)	0.01	–	0.0005
Initial kerogen porosity	0.1	–	0.01
Initial kerogen permeability (m²)	5.0×10^{-21}	–	5.0×10^{-21}
Kerogen compressibility (Pa^{-1})	1.06×10^{-10}	–	–
Possion's ratio	SRD: 0.22 NSRD: 0.2	–	0.2
Biot coefficient of IM	SRD: 0.58 NSRD: 0.49	–	–
Biot coefficient of kerogen	0.60	–	–
Langmuir pressure (MPa)	4.48	–	4.48
Langmuir volume (m³/kg)	2.72×10^{-3}	–	2.72×10^{-3}
Langmuir sorption strain constant	0.002	–	0.002
Maximum horizontal stress (MPa)	41.6	–	41.6
Minimum horizontal stress (MPa)	37.3	–	37.3
Shale density (kg/m³)	2500	–	–
Kerogen density (kg/m³)	1280	–	–
Archie cementation index of IM	2.5	–	–
Archie cementation index of kerogen	5	–	–
Natural fracture porosity	–	0.45	–
Natural fracture permeability (m²)	–	1×10^{-15}	–
Compressibility of entire reservoir (Pa^{-1})	–	8.4×10^{-8}	–
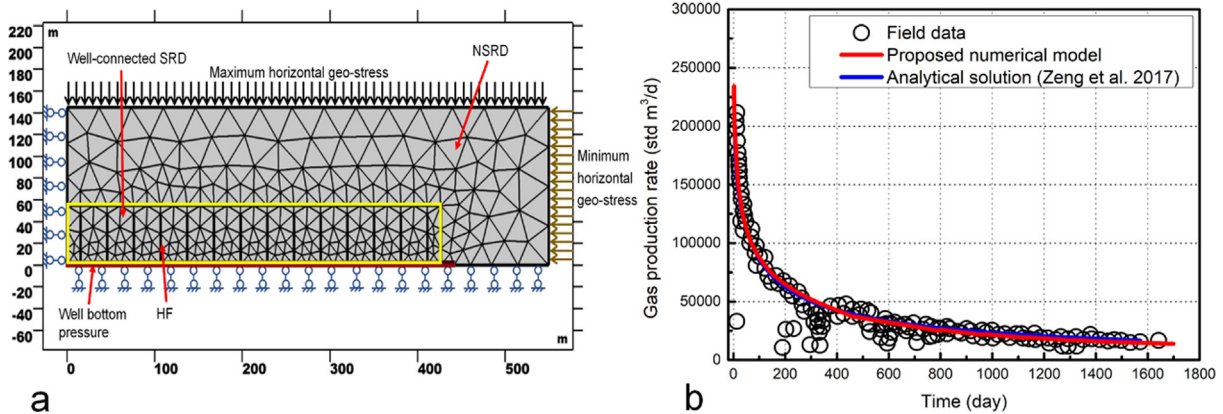
Fig. 8. Model validation and verification: Gas production in Barnett Shale with a continuous SRD. (a) Top view of the meshed quarter-geometry model and boundary conditions for Barnett Shale with a continuous SRD; (b) Comparison of the calculation results of the proposed model, the analytical model proposed by Zeng et al. [67], and the field data.
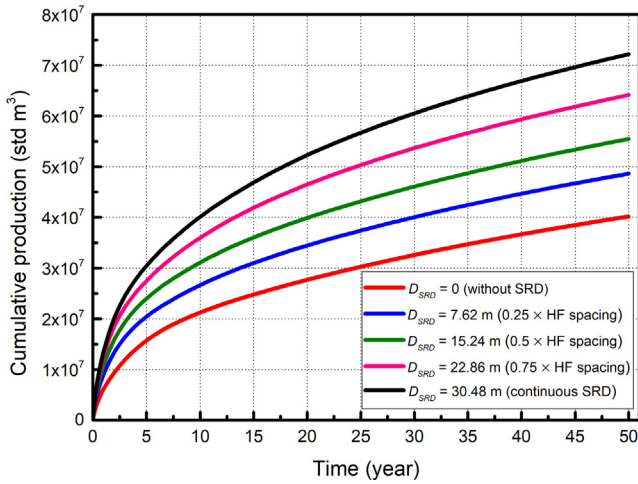
Fig. 9. Effect of sub-SRD width on 50-year cumulative production from Marcellus shale.

total recovery is near negligible, while that of the NSRD is only apparent in the late period of production [23,25]. In contrast, the SRD has both an abundant reserve and enhanced permeability, contributing a large proportion of gas to total production. Many previous studies suggest that in decades of extraction, the main source of gas production is the matrix near the HFs [10,13,24]. Our simulation results have confirmed that the gas depletion in the matrix mainly occurs in the SRD, as illustrated previously in Fig. 7. However, it must be noted from Fig. 7(c) that the pressure depletion in the NSRD after 50-years of production is also dramatic. Therefore, further investigating multi-domain effects on mass transfer during shale gas extraction is necessary. Towards this we first present the influences of size, initial porosity and permeability of the SRD, and then discuss the contributions of different domains to production to analyse this issue.

5.1.1. Effects of SRD size

In engineering practice, the SRD can be continuous or discontinuous and its size can be large or small, which depends on the cost and technical type/efficiency of hydraulic fracking. To study the effect of SRD size, we take different widths of a single sub-SRD surrounding a single HF (D_{SRD}) ranging from 0 to 30.5 m (the HF spacing) to conduct 50-year-production simulations based on a Marcellus shale reservoir, and obtain a series of cumulative gas production-time curves as shown in Fig. 9. This investigation of sensitivity on D_{SRD} covers various scenarios of SRD continuity including (1) Continuous SRD (D_{SRD} = 30.5 m); (2) Discontinuous SRD (0 < D_{SRD} < 30.5 m); and (3) Without SRD (D_{SRD} = 0). It is revealed in Fig. 9 that the impact of D_{SRD} on gas production is of significance. After 50 years, the cumulative production of the reservoir with a continuous SRD (7.22 × 10^7 standard m³) is nearly as twice that of a reservoir without an SRD (4.02 × 10^7 standard m³). A larger D_{SRD} means a greater size of the SRD domain with high porosity and permeability. Thus, the most readily-extracted gas occupies a higher proportion in the original gas in place (OGIP), benefiting gas production.

Another point related to SRD size is that, when a discontinuous SRD exists, gas depletion in the NSRD between sub-SRDs is faster than the situation without an SRD. To elucidate this phenomenon, IM pressure distributions after 2-year production in the reservoir, both with and without discontinuous SRD, are shown in Fig. 10(a) and (b), respectively. From this, it is apparent that IM pressure in the NSRD area between sub-SRDs (framed by the red dashed line) depletes more rapidly than that in the reservoir without SRD. That is, even if the SRD is not continuous, depletion in the NSRD near the HFs will be accelerated by the existence of the SRD, to some degree. The reason is that, with the rapid gas depletion of the SRD, the part of the NSRD between the sub-

SRDs is sandwiched by the low-pressure areas, accelerating gas extraction from this part. Clearly, this is an indirect effect on the SRD achieved by the mass transfer interactions between domains. However, this indirect enhancement effect is weaker than the enhancement effect of a continuous SRD, because it only performs by creating larger low-pressure areas around the high-pressure area instead of increasing porosity and permeability in the high-pressure area (as for a continuous SRD). Thus, it can be readily summarized that, for the enhancing effects of different SRD patterns on cumulative gas production of a shale reservoir, the following relation is valid:
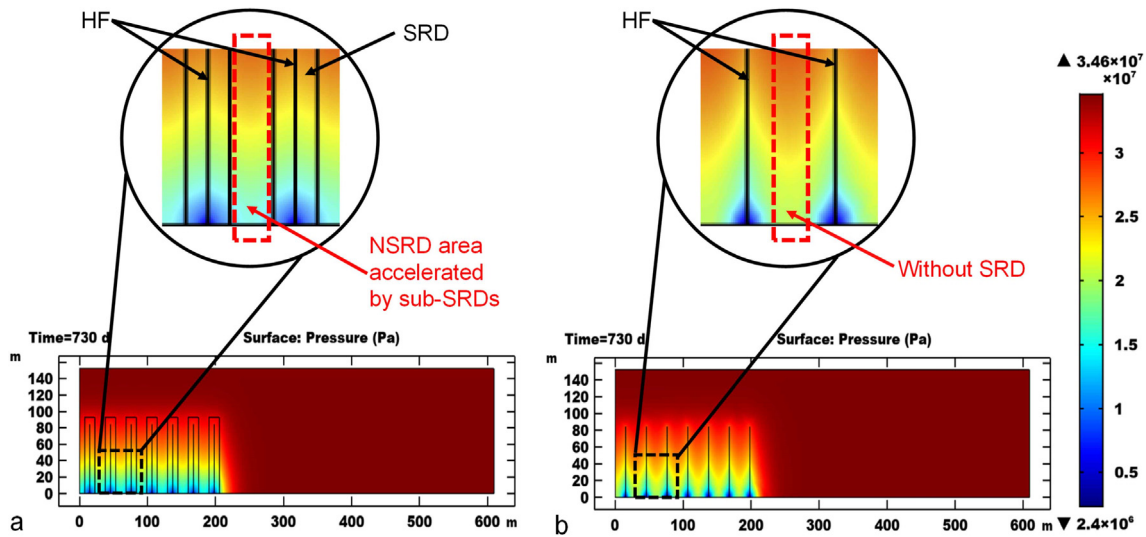
(HF + continuous SRD) > (HF + discontinuous SRD) > only HF

This relation is consistent with the 50-year production results shown in Fig. 9. In view of the strong direct/indirect enhancement effects of the SRD, generating a well-connected, continuous SRD *via* hydraulic fracking is crucial for shale gas production. If a continuous SRD is difficult to create due to the limits of cost/technique, we should at least widen the sub-SRDs as much as possible to increase the structural complexity of the near-HF matrix. In the remainder of this paper, we continue to discuss some other influencing factors based on the Marcellus shale reservoir case with a continuous SRD (D_{SRD} = 30.48 m).

5.1.2. Effects of initial porosity and permeability of SRD and NSRD

Initial basic properties such as porosity and permeability of SRD and NSRD also affect shale gas production. These properties can be considered as reflections of the internal structure of the domains [70]. For example, a complex pore/fracture network will tend to impart a high permeability. To investigate the effects of internal structures of shale matrix in different domains on production, initial IM porosities of SRD (ϕ_{m0}^{SRD}) and NSRD (ϕ_{m0}^{NSRD}) are respectively adjusted in numerical simulations with all other parameters fixed. As shown in Fig. 11(a), an increase of ϕ_{m0}^{SRD} (varying from 0.03 to 0.09) significantly enhances the 50-year cumulative production (from 4.99 × 10^7 to 9.36 × 10^7 standard m³). This can be ascribed to the increase of free gas storage in the SRD where gas can be easily extracted, and the enhancement of permeability in the SRD (according to the cubic law). Another reason of production enhancement is that the increase of porosity lowers the bulk compressibility of the IM in the SRD (C_m^{SRD}) according to the definition: $C_m = \alpha_m/(\phi_{m0} \cdot K_m)$, which will be discussed in Section 5.2 in detail. Conversely, the effect of increasing porosity of the IM in the NSRD on cumulative production is negligible in the first decade as shown Fig. 11(b). With the elapse of production time, the enhancement effect of increasing ϕ_{m0}^{NSRD} in the NSRD gradually becomes stronger, indicating the considerable dependence of late-stage gas production on the NSRD. An increase of ϕ_{m0}^{NSRD} from 0.03 to 0.09 leads to a 50-year production of 8.84 × 10^7 standard m³ which is 22.4% higher than that for ϕ_{m0}^{NSRD} = 0.03 (7.22 × 10^7 standard m³).

The effects of IM permeability in the SRD (k_{m0}^{SRD}) and IM permeability in the NSRD (k_{m0}^{NSRD}) on 50-year cumulative production are plotted in Fig. 12(a) and (b), respectively. With the increase of k_{m0}^{SRD} (from 1 × 10^{-19} to 2 × 10^{-18} m²), the cumulative production is dramatically enhanced (from 5.76 × 10^7 to 8.90 × 10^7 standard m³) - this is attributed to the enhancement of the SRD acceleration effect on gas depletion as mentioned previously (see Section 5.1.1). To the contrary, the enhancement effect on production caused by the increase of k_{m0}^{NSRD} is nearly negligible during the first 20 years because the permeability enhancement of the NSRD located in the deep part of the reservoir cannot affect the mass transfer in the SRD during early-stage production. Nevertheless, the improvement in production resulting from the increase of k_{m0}^{NSRD} becomes gradually greater with time in late stage production. After 50 years of production, the cumulative production for the reservoir with k_{m0}^{NSRD} = 2 × 10^{-18} m² reaches 8.64 × 10^7 standard m³ which is 20.8% higher than that for k_{m0}^{NSRD} = 1 × 10^{-19} m² (7.15 × 10^7 standard m³). This sensitivity study is based on the fact that hydraulic fracturing changes the basic properties of the SRD, and the degree of this change is dependent on the efficiency of hydraulic fracturing. Obviously, effective hydraulic

Fig. 10. Acceleration effect of SRD on NSRD depletion: (a) IM pressure distribution in the shale reservoir with a discontinuous SRD ($D_{SRD} = 15.24$ m) after 2-years production; (b) IM pressure distribution in the shale reservoir without SRD after 2-years production.

fracturing will greatly enhance ϕ_{m0}^{SRD} and k_{m0}^{SRD}, boosting gas production.

These results also confirm the validity of our 5-stage sequence of gas transport summarized in **Section 2.2**. That is, that the SRD and NSRD perform and contribute differently to production because of their property contrasts and different roles played in mass transfer. After the low pressure in the HF is formed in the first dozen days, the gas extracted in the first decade mainly comes from the SRD. In contrast, production from the NSRD is delayed by > 10 years for a significant pressure depletion in the SRD to induce substantial gas flow from the NSRD. Meanwhile, the NSRD usually has a large reserve which should not be neglected. The consequence of these observations is that the SRD controls the gas extraction process in the first years and decade, while the importance of the NSRD increases in late production. Clearly, if a model fails to include important complexities, including property contrasts and role conversion between different domains in the shale reservoir (similar to most of the previous models in which SRD and NSRD are not well-differentiated), the simulation results will not be reasonable.

5.1.3. Contributions of different domains to gas production

To further understand the various roles played by different domains in shale gas production, the contributions of different storage mechanisms in each domain to the cumulative production during 50-year

extraction are calculated and shown in Fig. 13**(a)**. More specifically, the modes of storage include: (1) Free gas in the HF; (2) Free gas in the IM in the SRD; (3) Free gas in kerogen in the SRD; (4) Adsorbed gas in kerogen in the SRD; (5) Free gas in the IM in the NSRD; (6) Free gas in kerogen in the NSRD; and (7) Adsorbed gas in kerogen in the NSRD. Clearly, each contribution changes with time. The contribution of the HF (the red line) is negligible due to its very small volume. In the SRD, free gas (the blue line is free gas in the IM, and the green line is that in the kerogen) provides the major source of cumulative production during 50 years. However, as time elapses, the contribution of free gas gradually decreases, while the contribution from adsorbed gas (pink line) becomes increasingly more important due to pressure-drop-induced desorption. Conversely, in the NSRD, both free-gas (the dark golden line is free gas in the IM, and the purple line is that in the kerogen) and adsorbed-gas (the purple line) contributions are incremental, demonstrating that the dominant role of the SRD is gradually displaced by that of the NSRD. These results again validate the 5-stage sequence of gas transport summarized in **Section 2.2**. Furthermore, the contributions of the HF, SRD and NSRD to cumulative production during 1-year, 10-years and 50-years of production are calculated based on the reduction of OGIPs in these domains, as shown in Fig. 13**(b)**. It can be clearly seen that the contribution of the HF is small at all times. The SRD is the main source of gas production during 50 years, while the
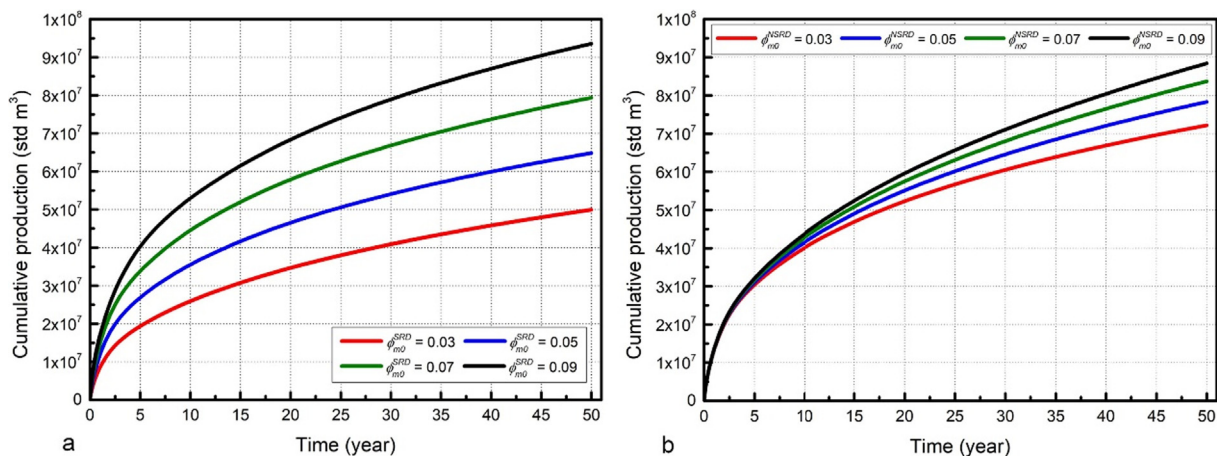
Fig. 11. Effects of initial IM porosity in different domains on 50-year cumulative production. (a) Changing the initial porosity of the SRD; (b) Changing the initial porosity of the NSRD.
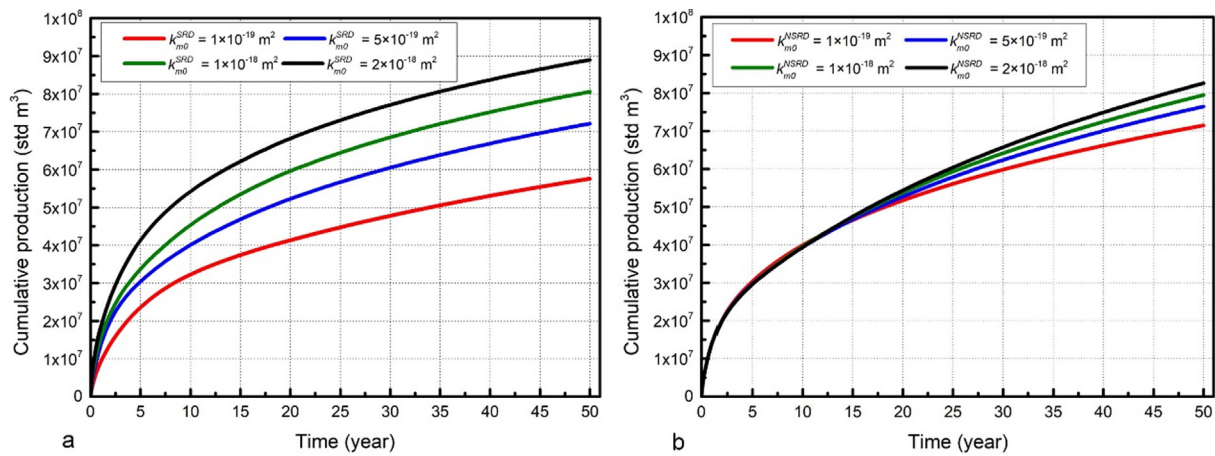
Fig. 12. Effects of initial IM permeability in different domains on 50-year cumulative production. (a) Changing the initial permeability of the SRD; (b) Changing the initial permeability of the NSRD.

importance of the NSRD increases with the depletion of the SRD pressure. In 1-year of production, 96% of the cumulative production is from the SRD, while the NSRD contribution is only 3.8%. In contrast, after 50 years, the contribution of the SRD drops to 75% and that of the NSRD correspondingly increases to as high as 25%.

The various roles played by different domains are also reflected by the contributions of the HF, SRD and NSRD to flow rate (daily production). The contributions of storage forms in different domains to flow rate shown in Fig. 14(a) reveals that the SRD provides most of the flow rate in the early period of production, while the contribution of the NSRD is of importance only in the late stage. For example, the gas supplied from free gas storage in the IM in the SRD accounts for 87.1% of the flow rate at 100 days, which is significantly higher than that from free gas in the IM in the NSRD (0.0004%). However, at 18,250 days, this contribution of the IM in the SRD to the flow rate drops to 38.7% which nearly equals that of the IM in the NSRD (37.9%). Moreover, the contributions of the three domains to flow rate at 1-year, 10-years and 50-years of production are given in Fig. 14(b) and again indicate the role conversion of domains. The HF contributes only a small amount of gas to the flow rate in the complete gas production process because of its small volume. At 1 year, the SRD provides 95.8% of daily production, much higher compared 4.2% offered by the NSRD. In contrast, at 50 years, the contributions of the SRD and the NSRD to daily production become equal (both are 50%).

In summary, multi-domain effects (caused by the fracturing-induced property contrasts in different domains and gas transport sequence in the full reservoir) lead to performance differences and role conversions of these domains during mass transfer during shale gas production. The HF provides a high-permeability flow channel from the reservoir to the wellbore, but gathers little gas volume. The SRD is the major gas source controlling the early decades of production, while its importance ultimately decreases with time. Correspondingly, the NSRD has only a minor influences on production in the early period, but gradually becomes crucial, and nearly as important as the SRD in the late period of the gas extraction process. Therefore, the NSRD is vital for the sustainability of gas production. These effects, often neglected in previous models, have been successfully incorporated in our model to improve the fidelity of simulation.

5.2. Multi-domain effects of mechanical deformation

The proposed model in this work is coupled by mechanical deformation within the entire shale formation - in addition to representing the mass transfer process, as noted in Section 3. More specifically, deformation of the matrix, including kerogen and IM in both the SRD and NSRD, is mechanically coupled by Eq. (9), while deformation-induced evolution in porosity, aperture and apparent permeability of the HF are described by Eqs. (47), (48) and (49), respectively. To investigate the multi-domain effects caused by mechanical coupling during shale gas extraction, we focus on the influence of varying compressibilities of HF and SRD on cumulative production and apparent permeability. The reason for conducting this investigation is
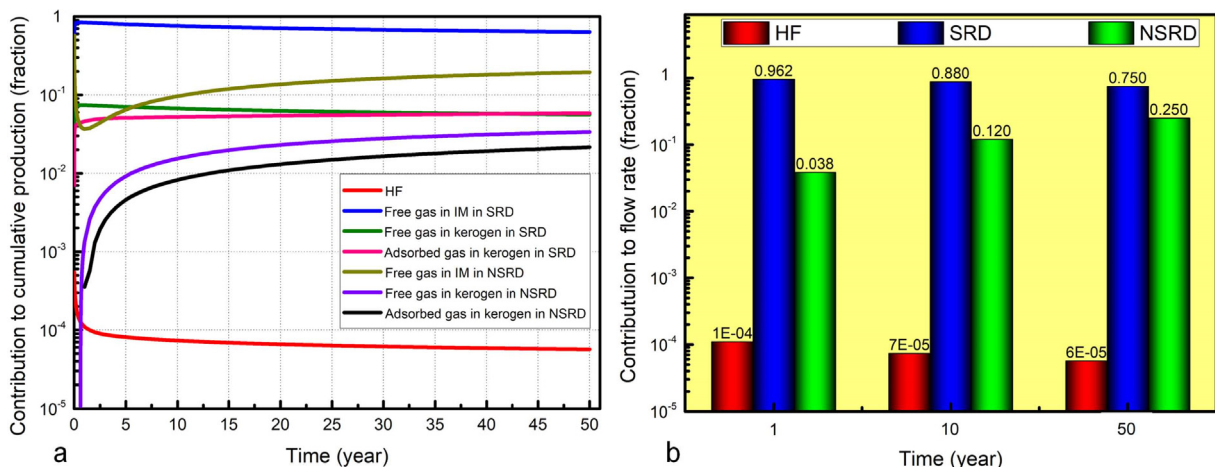

Fig. 13. Contributions of different domains to cumulative production. (a) Contributions of different storage forms in different domains to cumulative production; (b) Contributions of three domains to cumulative production after 1-year, 10-years and 50-years of production.
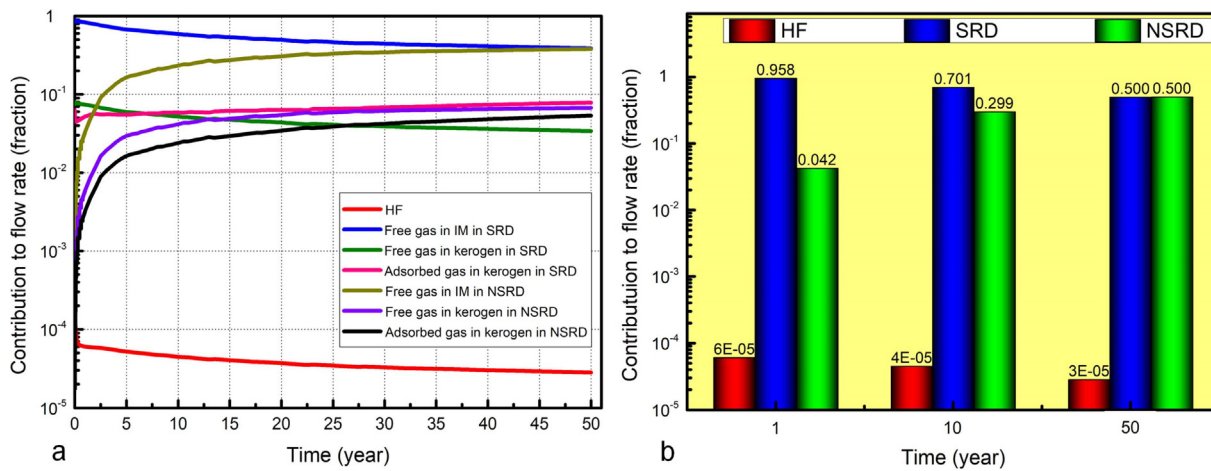
Fig. 14. Contributions of different domains to flow rate (daily production). (a) Contributions of different storage forms in different domains to flow rate; (b) Contributions of three domains to flow rate at 1-year, 10-years and 50-years.
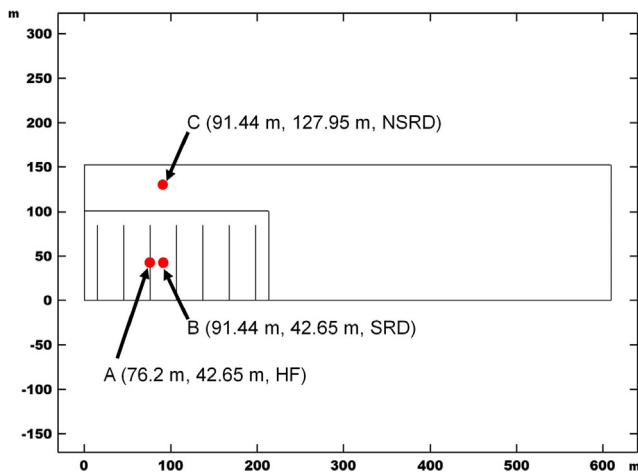

Fig.15. Points representing different domains in a reservoir in Marcellus shale: Point A – HF; Point B – SRD; Point C – NSRD.

that, hydraulic fracturing treatments tends to change the HF and SRD compressibilities. For a hydraulically fractured shale reservoir, HF compressibility depends significantly on the quality of proppant packing, and SRD compressibility is also different from that of the NSRD due to the improved matrix porosity and soaking of the fracking fluid. In this investigation, three representative points are selected in the geometry of a reservoir in Marcellus shale with a continuous SRD to investigate and compare the evolution in properties of different domains, as shown in Fig. 15. Point A represents an HF, Point B denotes the SRD and Point C is for the NSRD.

5.2.1. Effects of IM compressibility in the SRD

The effects of IM compressibility of the SRD (C_m^{SRD}) on cumulative gas production are presented in Fig. 16(a). This sensitivity study is based on the fact that hydraulic fracturing changes the bulk modulus (i.e., the compressibility) of the SRD, and the mabnitude of this change is dependent on the efficiency of the hydraulic fracturing treatment. As shown in Fig. 16 (a), increasing C_m^{SRD} from 1×10^{-10} to 1.5×10^{-8} Pa^{-1} results in a lower cumulative production (from 7.17×10^7 to 6.52×10^7 standard m^3) because the increased matrix compressibility intensifies shale compaction under the increasing effective stress, which decreases matrix porosity and permeability [39,47]. Furthermore, the effects of C_m^{SRD} on the evolution of IM apparent permeability in the SRD (k_{mapp}^{SRD}) are displayed in Fig. 16(b). When C_m^{SRD} is lower than 5×10^{-9} Pa^{-1}, The impact of effective stress is small and offset by effects

enhancing-permeability (including the sorption-induced strain and flow regime effect). Thus, k_{mapp}^{SRD} gradually increases with gas production for this case. However, when $C_m^{SRD} \geq 5 \times 10^{-9} Pa^{-1}$, the shale compaction effect that reduces matrix permeability is strong. In this case, the combined result of reservoir compaction and the effects enhancing permeability is that k_{mapp}^{SRD} first decreases then increases at later time. Moreover, a higher C_m^{SRD} implies a delayed rebound in permeability. For the case of $C_m^{SRD} = 5 \times 10^{-9} Pa^{-1}$, rebound of k_{mapp}^{SRD} occurs at 3.5 years, while for the case of $C_m^{SRD} = 1.5 \times 10^{-8} Pa^{-1}$, rebound is at 20.5 years.

Some previous studies (e.g., [39,47,71]) have discussed this permeability rebound phenomenon in unconventional gas reservoirs. However, most of their results are not obtained in a fully coupled multi-domain model. Compared to their models, one advantage of our model is that it can describe the difference in, and interactions between, various domains of the reservoir. As evidence of this, the evolution of apparent permeability of the HF with different C_m^{SRD}s are plotted in Fig. 16(c), and the evolution of apparent permeability of the IM in the NSRD with different C_m^{SRD}s are given in Fig. 16(d). It can be clearly seen that the change of the SRD compressibility affects permeability evolution in other domains as a result of the multi-domain interactions. Overall, an increased C_m^{SRD} results in lower permeabilities in both the HF and the NSRD. The changed C_m^{SRD} influences the strain distribution of the entire reservoir and thereby affects the progress of pressure depletion in the SRD and thus, permeability evolution in each domain. In consequence, the shape of the apparent permeability-time curve distinctly differs from one domain to another. For instance, permeability rebound is not observed in the HF during the 50-year production, as shown in Fig. 16(c), while it appears much earlier in the NSRD (at approximately 2 year) than in the SRD, as shown in Fig. 16(d).

5.2.2. Effects of HF compressibility

The influence of HF compressibility (C_f) on the 50-year cumulative production is presented in Fig. 17(a), indicating that higher C_f results in lower cumulative production. This is because the higher C_f intensifies the gradual closure of the HFs under an elevated (compressive) effective stress. The effects of C_f on k_{fapp} shown in Fig. 17(b) suggest that HF permeability may significantly decline with closure. When $C_f = 1 \times 10^{-10} Pa^{-1}$, HF closure is not significant, and k_{fapp} remains nearly constant during the 50-year production. In contrast, when $C_f = 1.5 \times 10^{-8} Pa^{-1}$, the k_{fapp} decreases significantly. After 50-year production, k_{fapp} diminishes as low as to 50% of its initial value, and further decreases as production continues. These indicate that, although HF only provides a small amount of stored gas for extraction (as discussed in Section 5.1.3), it plays a crucial role in shale gas production by inducing gas flow out from the shale. As a channel connecting matrix
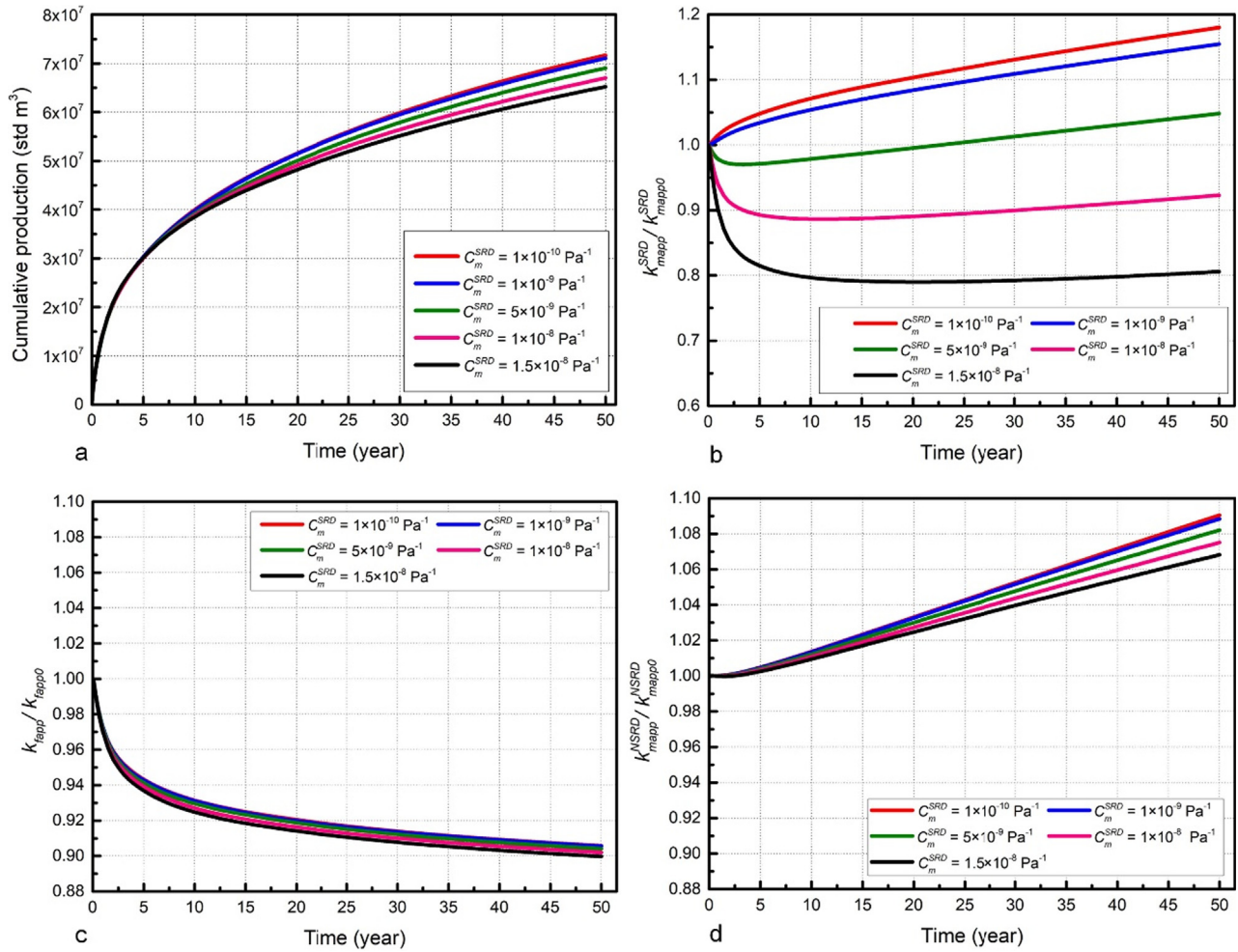
Fig. 16. Effects of IM compressibility in the SRD on cumulative production and permeability evolutios in different domains during 50-year production. (a) Effect on cumulative production; (b) Effect on IM apparent permeability evolution in the SRD; (c) Effect on HF apparent permeability evolution; (d) Effect on IM apparent permeability evolution in the NSRD.

and wellbore, the permeability of the HF is strongly influenced by the mechanical deformation of the shale reservoir.

Due to the coupled mechanical interactions between different domains, the change oin HF compressibility also affects permeability evolution in the SRD and the NSRD. The effects of C_f on permeability in the SRD and the NSRD during 50-years of extraction are plotted in Fig. 17(c) and (d), respectively. Overall, the increased C_f results in a smaller increase in permeability during production in both the SRD and NSRD by changing strain distribution of these two domains. Moreover, this effect in the NSRD is weaker than in the SRD. This is because the SRD directly contacts the HFs, while the NSRD does not contact the HFs. The changed C_f directly influences the SRD by HF-SRD interactions, and indirectly affects the NSRD by SRD-NSRD interactions.

These results, related to rock compressibility, demonstrate that the fracking-induced change of mechanical properties of the SRD and the HF influence the evolutions of transport properties in the entire reservoir. Thus, coupled mechanical deformation should be considered in shale reservoir simulations to prevent overestimating cumulative production. In addition, the change of mechanical properties in one domain will affect the permeability evolution in the entire shale reservoir as driven by the mechanical compatibility enforced between different domains. These results also reiterate the necessity of high-quality proppant packing for hydraulic fracturing treatments to prevent severe closure of the HF.

6. Conclusions

In this study, a fully coupled multi-domain and multi-physics model is developed to evaluate gas extraction processes from shale reservoirs. The processes in each domain (SRD – stimulated reservoir domain; NSRD – non-stimulated reservoir domain; HF – primary hydraulic fractures) are modelled, while the complexities of interactions between different domains and components are incorporated through cross-coupling relations of mass transfer and mechanical deformation. These PDEs were numerically solved by using the finite element method, and verified against analytical solutions and field observations. Based on our model results, the following conclusions can be drawn:

(1) Both SRD size and internal structure play key roles in shale gas production. The size is directly related to the cost of stimulation while the internal structure is determined by the stimulation technique. Different stimulation treatments may create different patterns of fractures in SRDs, which are reflected by the property contrasts that develop between SRDs and NSRDs. Our model results illustrate that complex internal structures of SRDs are favourable for gas production.

(2) From the perspective of mass transfer, an SRD enhances gas production in two ways. One is by directly improving gas flow capacity by enhancing porosity and permeability in the SRD. The other is by indirectly accelerating gas depletion in the NSRD by creating low-pressure zones around the NSRD.
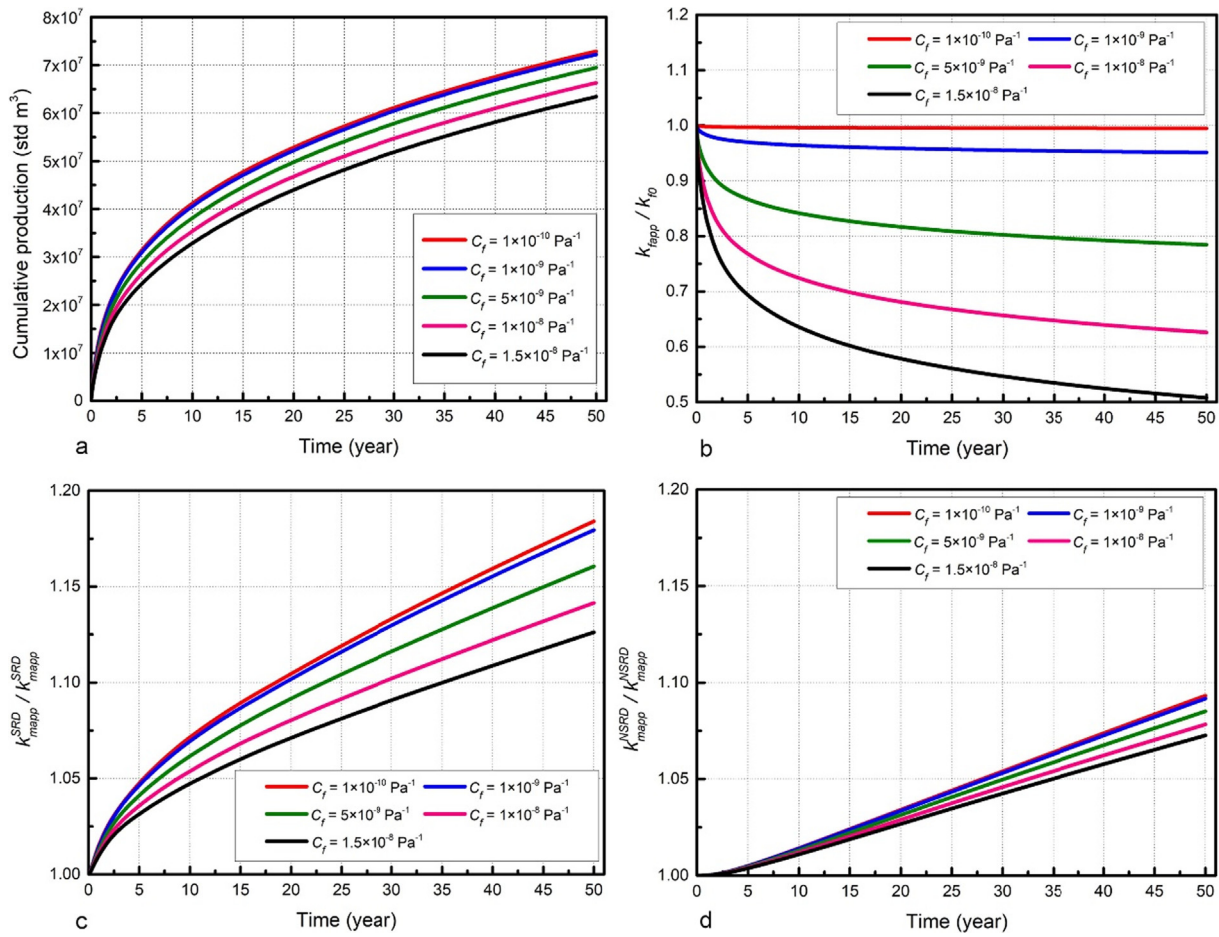
Fig. 17. Effects of HF compressibility on cumulative production and permeability evolution in different domains during 50-years of production. (a) Effect on cumulative production; (b) Effect on HF apparent permeability evolution; (c) Effect on IM apparent permeability evolution in the SRD; (d) Effect on IM apparent permeability evolution in the NSRD.

(3) HF, SRD and NSRD play different roles respectively in shale gas extraction, due to their property contrasts and sequential orders of gas transport. The HF provides a high-permeability flow channel connecting matrix and wellbore, while the role conversion between SRD and NSRD determines the long-term sustainability of gas production.

(4) The change in mechanical properties in one domain affects the evolution of transport properties throughout the entire reservoir. Deformation in shale caused by gas pressure depletion in different domains associated with mechanical property contrasts influences the effective strain distribution throughout the entire shale reservoir. Subsequently, permeability in each domain evolves with time and space. Eventually, permeability evolution in all domains determines the gas production.

CRediT authorship contribution statement

Wai Li: Methodology, Investigation, Writing - original draft. Jishan Liu: Supervision, Writing - review & editing. Jie Zeng: Conceptualization, Visualization. Yee-Kwong Leong: Supervision, Conceptualization. Derek Elsworth: Supervision, Writing - review & editing. Jianwei Tian: Methodology. Lin Li: Methodology.

Declaration of Competing Interest

The authors declare that they have no known competing financial interests or personal relationships that could have appeared to influence the work reported in this paper.

Acknowledgements

Appendix. A: Calculation of gas density and viscosity

For a given medium i ($i = k$ for kerogen; $i = m$ for IM and $i = f$ for HF), the gas density ρ_{gi} can be calculated by using the real gas equation of state:

$$\rho_{gi} = \frac{M}{Z_i RT} p_i \tag{A1}$$

where M is the gas molar weight, 0.016 kg/mol; R is the universal gas constant, 8.314 J/(mol·K); T is the reservoir temperature; p_i is the pore pressure in medium i; Z_i is the deviation factor of real gas in medium i, which is calculated by the empirical formula proposed by Mahmoud [72]:

$$Z_i = 0.702(p_{pri})^2 \exp(-2.5T_{pri}) - 5.524 p_{pri} \exp(-2.5T_{pri}) + 0.044(T_{pri})^2 - 0.164T_{pri} + 1.15 \tag{A2}$$

where $p_{pri} = p_i / p_c$ is a pressure ratio, p_c is the critical pressure of methane, 4.6×10^6 Pa. $T_{pri} = T_i / T_c$ is a temperature ratio, and T_c is the critical temperature of methane, 190.74 K.

Gas viscosity μ_i in medium i is determined by using the empirical formula proposed by Lee et al. [73]:

$$\mu_i = 10^{-7} \cdot \frac{(9.379 + 0.01607M) \cdot (1.8T)^{1.5}}{209.2 + 19.26M + 1.8T}$$

$$\cdot \exp\left\{ \left(3.448 + \frac{986.4}{1.8T} + 0.01009M\right) \cdot (10^{-3}\rho_{gi})^{\left[2.447 - 0.2224 \cdot \left(3.448 + \frac{986.4}{1.8T} + 0.01009M\right)\right]} \right\} \tag{A.3}$$

Appendix B:. Calculation of Knudsen number

Knudsen number Kn_i in medium i is defined as ($i = k$ for kerogen and $i = m$ for IM):

$$Kn_i = \frac{\lambda_i}{L_i} \tag{B1}$$

where λ_i is the mean free path of a single gas molecule and L_i is the characteristic scale of medium i. For kerogen with nano-capillary pores, $L_k = r_{k,stress,ads}$ [see Eq. (27)]; for IM with slot-shape fractures, $L_m = b_{m,stress}$ [see Eq. (35)]. λ_i can be calculated according to the formula proposed by Civan et al. [57]:

$$\lambda_i = \frac{\mu_i}{p_i} \sqrt{\frac{\pi Z_i RT}{2M}} \tag{B2}$$

References

[1] Li YF, Sun W, Liu XW, Zhang DW, Wang YC, Liu ZY. Study of the relationship between fractures and highly productive shale gas zones, Longmaxi Formation, Jiaoshiba area in eastern Sichuan. Pet Sci 2018;15(3):498–509. https://doi.org/10.1007/s12182-018-0249-7.

[2] Sakhaee-Pour A, Bryant S. Gas permeability of shale. SPE Reservoir Eval Eng 2012;15(4):401–9. https://doi.org/10.2118/146944-PA.

[3] Ziarani AS, Aguilera R. Knudsen's permeability correction for tight porous media. Transp Porous Media 2012;91:239–60. https://doi.org/10.1007/s11242-011-9842-6.

[4] Du DF, Wang YY, Zhao YW, Sui PS, Xia X. A new mathematical model for horizontal wells with variable density perforation completion in bottom water reservoirs. Pet Sci 2017;14(2):383–94. https://doi.org/10.1007/s12182-017-0159-0.

[5] Ding YD, Wu YS, Farah N, Wang C, Bourbiaux B. Numerical simulation of low permeability unconventional gas reservoirs. Proceedings of SPE/EAGE European Unconventional Resources Conference and Exhibition, 25-27 February, Vienna, Austria; 2014. doi:10.2118/167711-MS.

[6] Li W, Liu J, Zeng J, Tian J, Li L, Zhang M, Jia J, Li YF, Peng H, Zhao XH, Jiang JW. A critical review of the application of nanomaterials in frac fluids: The state of the art and challenges. Proceedings of SPE Middle East Oil and Gas Show and Conference, 18-21 March, Manama, Bahrain; 2019. doi:10.2118/195029-MS.

[7] Cao P, Liu J, Leong YK. General gas permeability model for porous media: Bridging the gaps between conventional and unconventional natural gas reservoirs. Energy Fuels 2016;30:5492–505. https://doi.org/10.1021/acs.energyfuels.6b00683.

[8] Cipolla CL, Lolon EP, Erdle JC, Rubin B. Reservoir modeling in shale-gas reservoirs. SPE Reservoir Eval Eng 2010;13:638–53. https://doi.org/10.2118/125530-PA.

[9] Wu YS, Li J, Ding D, Wang C, Di Y. A generalized framework model for the simulation of gas production in unconventional gas reservoirs. SPE J 2014;19(5):845–57. https://doi.org/10.2118/163609-PA.

[10] Yu W, Sepehrnoori K. Simulation of gas desorption and geomechanics effects for unconventional gas reservoirs. Fuel 2014;116:455–64. https://doi.org/10.1016/j.fuel.2013.08.032.

[11] Peng Y, Liu J, Pan Z, Connell LD. A sequential model of shale gas transport under the influence of fully coupled multiple processes. J Nat Gas Sci Eng 2015;27:808–21. https://doi.org/10.1016/j.jngse.2015.09.031.

[12] Wang J, Luo H, Liu H. An integrative model to simulate gas transport and production coupled with gas adsorption, non-Darcy flow, surface diffusion, and stress dependence in organic-shale reservoirs. SPE J 2017;22(1):244–64. https://doi.org/10.2118/174996-PA.

[13] Wei M, Liu J, Elsworth D, Wang E. Triple-porosity modelling for the simulation of multiscale flow mechanisms in shale reservoirs. Geofluids 2018. https://doi.org/10.1155/2018/6948726.

[14] Moghanloo RG, Javadpour F. Applying method of characteristics to determine pressure distribution in 1D shale-gas samples. SPE J 2014;19(3):361–72. https://doi.org/10.2118/168218-PA.

[15] Gong J, Rossen WR. Modeling flow in naturally fractured reservoirs: effect of fracture aperture distribution on dominant sub-network for flow. Pet Sci 2017;14(1):138–54. https://doi.org/10.1007/s12182-016-0132-3.

[16] Sondergeld CH, Ambrose RJ, Energy D, Rai CS Moncrieff J. Micro-structural studies of gas shales. Proceedings of SPE Unconventional Gas Conference, 23-25 February, Pittsburgh, Pennsylvania, USA; 2010. doi:10.2118/131771-MS.

[17] Vega B, Dutta A, Kovscek AR. CT imaging of low-permeability, dual-porosity systems using high x-ray contrast gas. Transp Porous Media 2014;101(1):81–97. https://doi.org/10.1007/s11242-013-0232-0.

[18] Wei M, Liu Y, Liu J, Elsworth D, Zhou F. Micro-scale investigation on coupling of gas diffusion and mechanical deformation of shale. J Petrol Sci Eng 2019;175:961–70. https://doi.org/10.1016/j.petrol.2019.01.039.

[19] Wu K, Li X, Wang C, Chen Z, Yu W. A model for gas transport in microfractures of shale and tight gas reservoirs. AIChE J 2015;61(6):2079–88. https://doi.org/10.1002/aic.14791.

[20] Cao P, Liu J, Leong YK. Combined impact of flow regimes and effective stress on the evolution of shale apparent permeability. J Unconvent Oil Gas Resour 2016;14:32–43. https://doi.org/10.1016/j.juogr.2016.01.004.

[21] Liu J, Wang JG, Gao F, Leung CF, Ma Z. A fully coupled fracture equivalent continuum-dual porosity model for hydro-mechanical process in fractured shale gas reservoirs. Comput Geotech 2019;106:143–60. https://doi.org/10.1016/j.compgeo.2018.10.017.

[22] Yuan B, Su Y, Moghanloo RG, Rui Z, Wang W, Shang Y. A new analytical multilinear solution for gas flow toward fractured horizontal wells with different fracture intensity. J Nat Gas Sci Eng 2015;23:227–38. https://doi.org/10.1016/j.jngse.2015.01.045.

[23] Brown M, Ozkan E, Raghavan R, Kazemi H. Practical solutions for pressure-transient responses of fractured horizontal wells in unconventional shale reservoirs. SPE Reservoir Eval Eng 2011;14(6):663–76. https://doi.org/10.2118/125043-PA.

[24] Cao P, Liu J, Leong YK. A fully coupled multiscale shale deformation-gas transport model for the evaluation of shale gas extraction. Fuel 2016;178:103–17. https://doi.org/10.1016/j.fuel.2016.03.055.

[25] Stalgorova K, Mattar L. Analytical model for unconventional multifractured composite systems. SPE Reservoir Eval Eng 2013;16(3):246–56. https://doi.org/10.2118/162516-PA.

[26] Wang J, Liu H, Wang L, Zhang H, Luo H, Gao Y. Apparent permeability for gas transport in nanopores of organic shale reservoirs including multiple effects. Int J Coal Geol 2015;152:50–62. https://doi.org/10.1016/j.coal.2015.10.004.

[27] Chen D, Pan Z, Ye Z. Dependence of gas shale fracture permeability on effective stress and reservoir pressure : Model match and insights. Fuel 2015;139:383–92. https://doi.org/10.1016/j.fuel.2014.09.018.

[28] Mi L, Jiang H, Cao Y, Fang S, Liu H, Zhou Y, et al. Comprehensive apparent permeability model coupled shale gas transfer mechanisms in natural fractures and matrix. J Petrol Sci Eng 2019;172:878–88. https://doi.org/10.1016/j.petrol.2018.08.080.

[29] Cui G, Liu J, Wei M, Feng X, Elsworth D. Evolution of permeability during the process of shale gas extraction. J Nat Gas Sci Eng 2017;49:94–109. https://doi.org/10.1016/j.jngse.2017.10.018.

[30] Akkutlu IY, Fathi E. Multiscale gas transport in shales with local kerogen heterogeneities. SPE J 2012;17(4):1002–11. https://doi.org/10.2118/146422-PA.

[31] Pang Y, Soliman MY, Deng H, Emadi H. Analysis of effective porosity and effective permeability in shale-gas reservoirs with consideration of gas adsorption and stress effects. SPE J 2017;22(6):1739–59.

[32] Civan F. Effective correlation of apparent gas permeability in tight porous media. Transp Porous Media 2010;82:375–84. https://doi.org/10.1007/s11242-009-9432-z.

[33] Wu K, Li X, Guo C, Wang C, Chen Z. A unified model for gas transfer in nanopores of shale-gas reservoirs: Coupling pore diffusion and surface diffusion. SPE J 2016;21(5):1583–611. https://doi.org/10.2118/2014-1921039-PA.

[34] Gu F, Chalaturnyk R. Permeability and porosity models considering anisotropy and discontinuity of coalbeds and application in coupled simulation. J Petrol Sci Eng

2010;74:113–31. https://doi.org/10.1016/j.petrol.2010.09.002.

[35] Sun Z, Li X, Shi J, Zhang T, Sun F. Apparent permeability model for real gas transport through shale gas reservoirs considering water distribution characteristic. Int J Heat Mass Transfer 115: 1008–1019. doi:10.1016/j.ijheatmasstransfer.2017.07.123.

[36] Warren JE, Root PJ. The behavior of naturally fractured reservoirs. Soc Petrol Eng J 1963;3(3):245–55. https://doi.org/10.2118/426-PA.

[37] Zhang Q, Wang WD, Kade Y, Wang BT, Xiong L. Analysis of gas transport behavior in organic and inorganic nanopores based on a unified apparent gas permeability model. Pet Sci 2020;17(1):168–81. https://doi.org/10.1007/s12182-019-00358-4.

[38] Detournay E, Cheng AHD. Fundamentals of Poroelasticity. Oxford 1993;Pergamon:113–71. https://doi.org/10.1016/B978-0-08-040615-2.50011-3.

[39] Zhang H, Liu J, Elsworth D. How sorption-induced matrix deformation affects gas flow in coal seams: A new FE model. Int J Rock Mech Min Sci 2008;45(8):1226–36. https://doi.org/10.1016/j.ijrmms.2007.11.007.

[40] Berryman JG. Extension of poroelastic analysis to double-porosity materials: new technique in microgeomechanics. J Eng Mech 2002;128(8):840–7. https://doi.org/10.1061/(ASCE)0733-9399(2002)128:8(840).

[41] Mehrabian A, Abousleiman YN. Gassmann equations and the constitutive relations for multiple-porosity and multiple-permeability poroelasticity with applications to oil and gas shale. Int J Numer Anal Meth Geomech 2015;39(14):1547–69. https://doi.org/10.1002/nag.2399.

[42] Rezaee R. Fundamentals of Gas Shale Reservoirs. John Wiley & Sons; 2015.

[43] Yan F, Han DH. Measurement of elastic properties of kerogen. SEG Technical Program Expanded Abstracts 2013;2013:2778–82. https://doi.org/10.1190/segam2013-1319.1.

[44] Islam MA, Skalle P. An experimental investigation of shale mechanical properties through drained and undrained test mechanisms. Rock Mech Rock Eng 2013;46:1391–413. https://doi.org/10.1007/s00603-013-0377-8.

[45] Adelinet M, Dominguez C, Fortin J, Violette S. Seismic-refraction field experiments on Galapagos Islands: A quantitative tool for hydrogeology. J Appl Geophys 2018;148:139–51.

[46] Ross DJK, Bustin RM. Impact of mass balance calculations on adsorption capacities in microporous shale gas reservoirs. Fuel 2007;86:2696–706. https://doi.org/10.1016/j.fuel.2007.02.036.

[47] Cui X, Bustin AMM, Bustin RM. Measurements of gas permeability and diffusivity of tight reservoir rocks: different approaches and their applications. Geofluids 2009;9:208–23. https://doi.org/10.1111/j.1468-8123.2009.00244.x.

[48] Moridis GJ, Blasingame TA, Freeman CM (2010). Analysis of mechanisms of flow in fractured tight-gas and shale-gas reservoirs. Proceedings of SPE Latin American and Caribbean Petroleum Engineering Conference, 1-3 December, Lima, Peru. doi:10.2118/139250-MS.

[49] Cui X, Bustin RM. Volumetric strain associated with methane desorption and its impact on coalbed gas production from deep coal seams. AAPG Bull 2005;89:1181–202. https://doi.org/10.1306/05110504114.

[50] Jiang J, Yang J. Coupled fluid flow and geomechanics modeling of stress-sensitive production behavior in fractured shale gas reservoirs. Int J Rock Mech Min Sci 2018;101:1–12. https://doi.org/10.1016/j.ijrmms.2017.11.003.

[51] Palmer I, Mansoori J. How permeability depends on stress and pore pressure in coalbeds: a new model. SPE Reservoir Eval Eng 1998;1:539–44. https://doi.org/10.2118/52607-PA.

[52] Bird RB, Stewart WE, Lighfoot EN (2002). Transport Phenomena. 2nd Edition, New York: John Wiley & Son. doi:10.1115/1.1424298.

[53] Archie GE. The electrical resistivity log as an aid in determining some reservoir characteristics. Transactions of the AIME. 1942;146:54–62. https://doi.org/10.2118/942054-G.

[54] Iversen N, Jorgensen BB. Diffusion coefficients of sulfate and methane in marine sediment: Influence of porosity. Geochim Cosmochim Acta 1993;57:571–8. https://doi.org/10.1016/0016-7037(93)90368-7.

[55] Riewchotisakul S, Akkutlu IY. Adsorption-enhanced transport of hydrocarbons in organic nanopores. SPE J 2016;21(6):1960–9. https://doi.org/10.2118/175107-PA.

[56] Beskok A, Karniadakis GE. Report: A model for flows in channels, pipes, and ducts at micro and nano scales. Microscale Thermophys Eng 1999;3(1):43–77. https://doi.org/10.1080/108939599199864.

[57] Civan F, Rai CS, Sondergeld CH. Shale-gas permeability and diffusivity inferred by improved formulation of relevant retention and transport mechanisms. Transp Porous Media 2011;86(3):925–44. https://doi.org/10.1007/s11242-010-9665-x.

[58] Civan F, Rai CS, Sondergeld CH. Determining shale permeability to gas by simultaneous analysis of various pressure tests. SPE J 2012;17(3):717–26. https://doi.org/10.2118/144253-PA.

[59] Wang J, Chen L, Kang Q, Rahman SS. Apparent permeability prediction of organic shale with generalized lattice Boltzmann model considering surface diffusion effect. Fuel 2016;181:478–90. https://doi.org/10.1016/j.fuel.2016.05.032.

[60] Naraghi ME, Javadpour F, Ko LT. An object-based shale permeability model: Non-darcy gas flow, sorption, and surface diffusion effects. Transp Porous Media. 125 (1): 23–39. doi:10.1007/s11242-017-0992-z.

[61] Kazemi H, Gilman JR, Elsharkawy AM. Analytical and numerical solution of oil recovery from fractured reservoirs with empirical transfer functions (includes associated papers 25528 and 25818). SPE Reservoir Eng 1992;7(2):219–27. https://doi.org/10.2118/19849-PA.

[62] Pan Z, Connell LD. Modelling permeability for coal reservoirs: A review of analytical models and testing data. Int J Coal Geol 2012;92:1–44. https://doi.org/10.1016/j.coal.2011.12.009.

[63] Yu W, Zhang T, Du S, Sepehrnoori K. Numerical study of the effect of uneven proppant distribution between multiple fractures on shale gas well performance. Fuel 2015;142:189–98. https://doi.org/10.1016/j.fuel.2014.10.074.

[64] Cao P, Liu J, Leong YK. A multiscale-multiphase simulation model for the evaluation of shale gas recovery coupled the effect of water flowback. Fuel 2017;199:191–205. https://doi.org/10.1016/j.fuel.2017.02.078.

[65] Zhou Y, Nikoosokhan S, Engelder T. Sonic properties as a signature of overpressure in the Marcellus gas shale of the Appalachian Basin. Geophysics 2017;82(4):D235–49. https://doi.org/10.1190/geo2016-0547.1.

[66] Ward J (2010). Kerogen density in the Marcellus shale. Proceedings of SPE Unconventional Gas Conference, 23-25 February, Pittsburgh, Pennsylvania, USA. doi:10.2118/131767-MS.

[67] Zeng J, Wang X, Guo J, Zeng F. Composite linear flow model for multi-fractured horizontal wells in heterogeneous shale reservoir. J Nat Gas Sci Eng 2017;38:527–48. https://doi.org/10.1016/j.jngse.2017.01.005.

[68] Pan Z, Connell LD. Reservoir simulation of free and adsorbed gas production from shale. J Nat Gas Sci Eng 2015;22:359–70.

[69] Stankiewicz A, Bennett B, Wint O, Ionkina N, Motherwell B, Mastalerz M (2015). Kerogen density revisited–lessons from the Duvernay Shale. Proceedings of Unconventional Resources Technology Conference, 20-22 July, San Antonio, Texas, USA. doi:10.15530/URTEC-2015-2157904.

[70] Nandlal K, Weijermars R. Drained rock volume around hydraulic fractures in porous media: planar fractures versus fractal networks. Pet Sci 2019;16(5):1064–85.

[71] Shi JQ, Durucan S. Drawdown induced changes in permeability of coalbeds: A new interpretation of the reservoir response to primary recovery. Transp Porous Media 2004;56:1–16. https://doi.org/10.1023/B:TIPM.0000018398.19928.5a.

[72] Mahmoud M. Development of a new correlation of gas compressibility factor (Z-factor) for high pressure gas reservoirs. J Energy Resour Technol 2014;136(1):012903https://doi.org/10.1115/1.4025019.

[73] Lee AL, Gonzalez MH, Eakin BE. The viscosity of natural gases. J Petrol Technol 1966;18(8):997–1000. https://doi.org/10.2118/1340-PA.